DISS. ETH NO. 30166

QUANTUM CORRELATIONS OF EXCITON–POLARITONS

A thesis submitted to attain the degree of
DOCTOR OF SCIENCES
(Dr. sc. ETH Zürich)

presented by
GIAN-MARCO SCHNÜRIGER

Master of Science ETH in Interdisciplinary Sciences,
ETH Zürich

born on 30.08.1990

accepted on the recommendation of

Prof. Dr. Ataç İmamoğlu
Prof. Dr. Jérôme Faist
Dr. Sylvain Ravets

2024

Cover image front: Second–order correlation function measured for a exciton like polariton ($|c_c|^2 = 0.28$) for different laser detunings $\Delta = \pm(0\,\Gamma p,\ 0.16\,\Gamma p,\ 0.25\,\Gamma p$ and $0.5\,\Gamma p)$ as a function of time τ. It shows the transition from antibunched polaritons on the red to bunched polaritons on the blue side.

Cover image back: Transmission spectrum as a function of the cavity length, showing the anticrossing and the lower and upper polariton branch, as well as a higher order optical mode on the top left.

Abstract

In this work we study the quantum nature of a hybrid light–matter system, where we use the interactions of the matter component to introduce a sizable nonlinearity to photons. It is a longstanding goal to achieve interactions that overcome the losses in the system, resulting in the photon blockade effect that leads to nonclassical signatures measurable in photon correlation experiments. To implement such a system we combine an optical cavity with excitons in an InGaAs quantum well where the strong light–matter coupling leads to new hybridised eigenstates called polaritons. To further enhance the existing interactions between these polaritons we introduce lateral confinement of the optical mode and a second quantum well. This allows for the coupling to indirect excitons, where the spatial separation of electrons and holes introduces dipolar interactions to the system.

In order to measure correlations over a wide range of polariton compositions, we use an open cavity design allowing for in situ tuning of the cavity length. This design naturally results in sizable fluctuations of the cavity length, directly translating to the energy of the optical resonance. We therefore developed a measurement procedure based on postselecting photon arrival times based on their countrate, allowing us to overcome these fluctuations and resolve the correlations of the polaritons.

The interactions between purely direct exciton–polaritons allowed for the first observation of nonclassical polariton correlations by continuous wave excitation, with a value $g^{(2)}(0) = 0.90(1)$ at an cavity content of 28 %, marking the current record for comparable systems. Correlation measurements at lower exciton fractions show the presence of a new regime, where a small antibunching persists independent of the detuning between the excitation laser and the polariton mode. This behaviour cannot be explained by polariton–polariton interactions. We attribute them to the presence of the biexciton

and propose a "dissipative blockade" mechanism, where the selective coupling of the biexciton to the doubly excited polariton state lowers the probability of the two-photon emission. The good agreement of the data with our numerical simulations strongly supports this mechanism as origin of the detuning independent antibunching. To our knowledge this would mark the first observation of nonclassical correlations originating from a dissipative blockade mechanism, and could potentially offer a novel approach to the creation of single-photon states. At the same time, the polariton interaction strengths extracted from the simulation depend much stronger on the exciton content as expected from the commonly used quadratic scaling law. And while we do not have an explanation for this behaviour, it suggests that a microscopic theory might be necessary to capture the details in the scaling of the interactions of these composite particles.

At the same time careful measurements of the polariton properties show that as a result of the increased indirect exciton content, the exciton oscillator strength is substantially reduced. This leads to a broadened linewidth and a lower transmission which limits the available parameter space. As a result, the expected interaction enhancement could not be observed in this system.

Kurzfassung

In dieser Arbeit untersuchen wir die Quantennatur von hybriden Licht-Materie Zuständen, in denen wir die Wechselwirkung des Materieanteils nutzen, um eine nennenswerte Nichtlinearität der Photonen zu erzeugen. Dabei ist es ein grundlegendes Ziel, ein Regime zu erreichen in dem die Wechselwirkungsstärke grösser ist, als die Verlustrate im System. Dies führt zu einer Photonenblockade, welche es uns erlaubt nicht-klassische Signaturen in Photonkorrelationsexperimenten zu messen. Wir realisieren solch ein System durch Kombination eines optischen Resonators mit Exzitonen in einem InGaAs-Quantentopf. Die starke Licht-Materie-Wechselwirkung erzeugt dabei neue, hybridisierte Eigenzustände, genannt Polaritonen. Um die existierenden Wechselwirkungen zwischen den Polaritonen weiter zu erhöhen, schränken wir die laterale Ausdehnung der Photonen ein und fügen einen zweiten Quantentopf hinzu. Dieser zweite Quantentopf erlaubt es uns indirekte Exzitonen zu erzeugen, welche durch die räumliche Trennung der Elektronen und Löcher dipolare Wechselwirkungen aufweisen.

Um die Photonkorrelationen über einen grossen Bereich von Polaritonzusammensetzungen messen zu können, benutzen wir einen optischen Resonator mit zwei unabhängig voneinander befestigten Spiegeln, der es uns erlaubt dessen Länge im Experiment zu variieren. Dieser Aufbau führt naturgemäss zu Fluktuationen der Länge und damit der Photonenergie. Deshalb haben wir eine Messprozedur entwickelt, die darauf basiert die Ankunftszeiten der Photonen in Relation zur momentanen Photonenzählrate zu selektieren. Diese Vorgehensweise erlaubt es uns trotz der Fluktuationen zuverlässige Korrelationen zu messen.

Die Wechselwirkungen zwischen direkten Polaritonen haben es uns erlaubt, die erste Messung von nichtklassischen Korrelationen in einem Dauerstrich Laser Experiment durchzuführen. Der dabei gemessene Wert von

$g^{(2)}(0) = 0.90(1)$ bei einem Photonenanteil von 28 % übertrifft die Ergebnisse von bisherigen Experimenten in vergleichbaren Systemen. Bei niedrigen Exzitonanteilen beobachten wir ein komplett neues Verhalten, bei dem schwache, nichtklassische Korrelationen unabhängig von der Verstimmung zwischen der Energie des Lasers und des Polaritonzustandes auftreten. Dieses Verhalten ist nicht alleinig durch Polaritonwechselwirkungen erklärbar und wir schlagen einen dissipativen Blockademechanismus vor. Dieser basiert auf der selektiven Kopplung zum Biexziton, das zu einer Verbreiterung des doppelt angeregten Polaritonzustands führt und dadurch die Wahrscheinlichkeit einer Zweiphotonenemission reduziert. Die gute Übereinstimmung zwischen unseren Daten und numerischen Simulationen unterstützt diese Vermutung. Nach unserem Wissensstand wäre das die erste Beobachtung von nichtklassischen Korrelationen durch solch einen dissipativen Blockademechanismus und könnte neue Möglichkeiten zur Erzeugung von Einzelphotonenzuständen eröffnen. Gleichzeitig finden wir, dass die Wechselwirkungsstärken, die wir von den Simulationen erhalten, stärker vom Exzitonanteil abhängen, als wir aufgrund der gängigen quadratischen Skalierung erwarten würden. Und obwohl wir keine Erklärung für diese Abhängigkeit haben, deutet sie darauf hin, dass die quadratische Formel nicht ausreicht um die Skalierung der zusammengesetzten Teilchen zu erklären und eine mikroskopische Theorie benötigt wird.

Die sorgfältige Messung der Polaritoneigenschaften zeigt, dass das Hinzufügen von indirekten Exzitonen die Oszillatorstärke stark reduziert. Die damit verbundene Linienverbreiterung und Reduktion der Transmission limitiert den verfügbaren Parameterraum beträchtlich und führt dazu, dass wir in diesem System keine Verstärkung der Polaritonwechselwirkungen feststellen konnten.

Contents

List of symbols and abbreviations

$\hbar$	reduced Planck constant
μ_0	vacuum permeability
c	speed of light in vacuum
e	elementary charge
h	Planck constant
m_e	electron mass
0D	zero-dimensional
1D	one-dimensional
2D	two-dimensional
APD	avalanche photodiode
CCD	charge-coupled device
CW	continuous wave
DBR	distributed Bragg reflector
FPGA	field-programmable gate array
FWHM	full width at half maximum
HBT	Hanbury Brown and Twiss
MBE	molecular beam epitaxy
ND	neutral-density

PID	proportional–integral–derivative controller
QW	quantum well
SSPD	superconducting nanowire single-photon detector
TCSPC	time-correlated single photon counting
tmm	transfer matrix method
VOA	variable optical attenuator

Chapter 1
Introduction

Photons have always been a key carrier of information, allowing us to observe the world and communicate over long distances. This is owed by a large degree to their inherent linear nature, allowing them to propagate without self interaction and therefore maintaining their initial information content. At the same time this also inherently limits their range of applications, as interactions are a key ingredient in information processing. Therefore, a long standing goal has been the achievement of interactions on the level of single photons [1], thereby realizing systems located in the top row of Fig. 1.1. In practice, strong photon–photon interactions would allow the creation of optical switches or transistors [2] and would open up new possibilities in quantum metrology [3, 4], quantum computation and quantum cryptography [5, 6].

Photons propagating inside a medium naturally experience nonlinear behaviour originating from higher-order terms in their polarizability ($\chi^{(2)}, \chi^{(3)}$). As the second-order term vanishes in many materials due to their symmetry, the third-order term is usually weak [7] and only the development of high-power lasers lead to the observation of nonlinear effects such as the generation of optical harmonics [8]. To significantly enhance the interactions, photons can be coupled coherently to matter excitations, which are inherently nonlinear. This hybridisation of light and matter states leads to the formation of new quasiparticles called polaritons [9], inheriting properties from both constituents. A common technique to achieve strong light–matter coupling is the usage of an optical cavity [10–12], allowing a photon to interact multiple times with the matter excitation during its lifetime, thereby boosting the effective light–matter interaction strength.

One type of matter excitation with beneficial optical properties which became widely used due to advances in semiconductor fabrication techniques

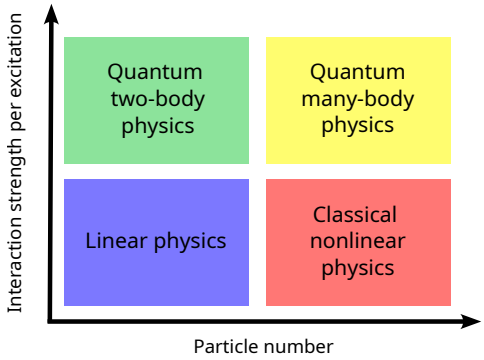

Figure 1.1: Classification of physical systems by their particle number and interaction strength, adapted from [1]. Crossing into the top/"quantum" row requires the interactions to be larger than the losses in the system.

are excitons [13, 14], bound electron–hole pairs in semiconductor quantum wells (QWs). Over the past two decades, a broad range of interesting phenomena have been displayed in exciton–polaritons, for example the observation of Bose–Einstein condensation [15], superfluidity [16], topological edge states [17], dissipative phase transitions [18, 19], vortex formation [20, 21] and dark solitons [22, 23]. While these experiments rely on the finite interactions between polaritons, their respective strength is comparatively small and the observed effects originate from collective phenomena that can be described by semi-classical models, placing them on the bottom right in Fig. 1.1.

To observe the true quantum nature of exciton–polaritons, the interactions have to overcome the natural loss rates in the system, allowing the creation of strongly correlated single- and multi-particle states. For single excitations, this manifests in the polariton blockade effect [24, 25] where the interaction leads to an anharmonicity in the excitation manifold, creating an effective two-level system analogous to a single atom inside a cavity [26]. The emerging single-photon Fock state is highly sought after in quantum information, quantum cryptography [5, 6], and quantum metrology [3, 4]. While there are already numerous schemes to create single photons [27, 28], like the already-mentioned single atom in a cavity [26], semiconductor quantum dots [29–31] or parametric downconversion [32], the high demands in

terms of low losses, distinguishability, high repetition rate, scalability, tunability and integrability still leave demand for new and improved sources. In addition to interesting single-particle phenomena, increasing the number of excitations in the regime of strong interactions allows the study of strongly correlated many-body phenomena. For example, the transition between superfluid and Mott insulator states in two-dimensional systems [33, 34] or the Tonks–Girardeau gas in one-dimensional systems [35], which have both been observed in ultracold atomic gases [36–38]. The driven-dissipative nature of exciton–polaritons would allow access to a different regime for quantum simulators [39], which would not easily be achieved using cold atoms.

There are two main strategies towards enhancing the effective interactions in exciton–polaritons: the introduction of an additional confinement and coupling to a separate state with strong correlations. One approach is inspired by cold atoms, where Feshbach resonances are a key element in tuning the interactions [40]. In excitonic systems the biexciton bound state is predicted to have the same effect [41]. Experiments at high polariton densities have shown the modification from repulsive to attractive interactions due to the coupling to the biexciton resonance [42] and recent experiments could verify the results at low densities by photon correlation measurements [43]. A different approach relies on the formation of indirect excitons in spatially separated QWs, which naturally have stronger interactions due to their permanent dipole. Electron tunneling allows for coherent coupling between the indirect and direct exciton, combining the dipolar interactions with the large oscillator strength. By measuring the interaction-induced blueshift [44], an interaction enhancement by a factor of 7.4 compared to direct excitons was observed. Another commonly used technique is the introduction of confinement for polaritons by tailoring either the excitonic or the photonic mode [45], which leads to a reduced interparticle distance and therefore increases their scattering rate. A prominent example for exciton confinement is the use of etching techniques to create pillar structures [46] which have shown significant interaction-induced blueshifts but suffer from relatively short polariton lifetime, partially due to the overlap of the polariton mode with the edges of the pillar structure. A promising approach for the confinement of photons is the combination of QWs with optical waveguides [47, 48], which additionally opens up the possibility to build optical circuits. Experiments in combination with dipolar excitons already showed sizable interactions and

optimisation of sample parameters could potentially provide access to the regime of strong interactions [49, 50]. While the photon confinement in optical waveguides is essentially limited to 1D, further confinement can be achieved with hemispherical cavities, allowing for the creation of a 0D photonic mode [51]. Hemispherical cavities based on curved fiber surfaces have been shown to provide excellent optical properties and in situ tunability of the resonator length [52, 53] and in combination with QW excitons allowed for the observation of the onset of nonclassical correlations [54, 55].

In this dissertation we combine the optical confinement of a fiber-based hemispherical cavity with the dipolar interactions from indirect excitons in a pair of coupled QWs. By measuring the correlations of the system [25] we can directly observe the potential quantum nature of polaritons and learn more about their dependence on various parameters.

Chapter 2

Exciton–polaritons

In this chapter we lay the theoretical foundation to describe polaritons composed of light–matter quasiparticles and their interactions. We show how we aim to increase these interactions by introducing lateral confinement and a dipolar moment through charge separation.

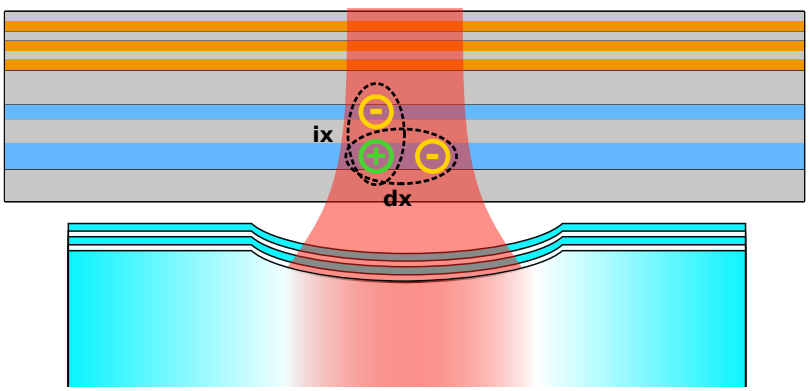

Figure 2.1: Conceptual illustration of direct and indirect excitons (dx/ix) coupled to photons within a hemispherical fiber cavity.

2.1 Excitons

Semiconductors are a class of materials with numerous attributes that make them desirable for research and applications. Their properties originate from the electronic band structure and they are generally defined by the location of the Fermi energy within the band gap, meaning that in the ground state the valence band is filled with electrons while the conduction band remains empty [56]. As electrons can be promoted from the valence to the conduction band by external means, the properties of the semiconductor can be controlled, which makes them a suitable building block for active devices. In general they are classified into direct and indirect band gap semiconductors, based on the location of the band gap minimum in momentum space. Photons do not couple directly to indirect band gap semiconductors, since they carry only a small momentum and additional processes are necessary to satisfy momentum conservation. In our work we are interested in the optical properties and therefore use direct band gap semiconductors, namely GaAs and InGaAs, which belong to the class of III–V semiconductors with a zinc blende crystal structure [57] shown in Fig. 2.2 **a**. Their band structure around the crystal momentum $k = 0$ along with their total angular momentum quantum numbers $|J, J_z\rangle$ are sketched in Fig. 2.2 **b**. It consists of a single conduction band with s-type symmetry and an effective mass $m_\mathrm{e}^* = 0.063\, m_\mathrm{e}$, and multiple valence bands with p-type symmetry that show a more complex structure. The so-called split-off band, separated due to spin–orbit coupling, has the lowest energy and can be neglected for the rest of this thesis, as the spin–orbit splitting is much larger than the light matter coupling. The remaining heavy and light hole bands are only degenerate at $k = 0$ and split off due to their different effective masses of $m_\mathrm{LH} = 0.082\, m_\mathrm{e}$ and $m_\mathrm{HH} = 0.51\, m_\mathrm{e}$ respectively.

By absorbing a photon the electrons in the valence band can be excited to the conduction band, leaving behind a vacancy in the otherwise filled valence band [58–60]. This vacancy can also be described as a positively charged particle with opposite spin and momentum and is commonly referred to as a hole. To reduce their energy, electron and hole can form a bound state due to their mutual Coulomb attraction, forming the so-called exciton. This quasiparticle made up from a single positive and a single negative charge can be described analogously to the Hydrogen atom, but due to the low

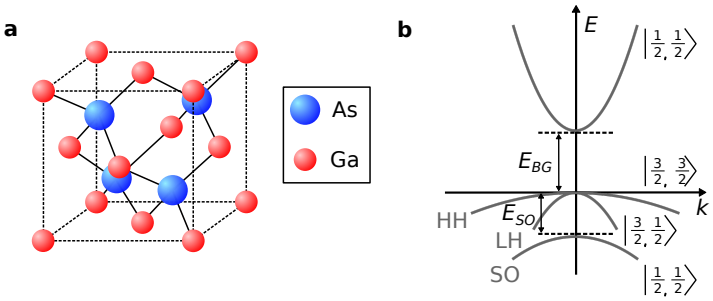

Figure 2.2: **a** Face-centred cubic lattice of the zinc blende crystal structure of GaAs. **b** Sketch of the GaAs band structure around $k = 0$, showing the single s-type symmetry conduction band and the different p-type valence bands with their total angular momentum quantum numbers $|J, J_z\rangle$. While the light and heavy hole (LH, HH) are degenerate at $k = 0$, the split-off band (SO) is $E_{\mathrm{SO}} = 0.34\,\mathrm{eV}$ lower in energy. Therefore the lowest energy transition is between LH/HH and the conduction band with $E_{\mathrm{BG}} = 1.42\,\mathrm{eV}$. The figure is inspired by [57] and the quoted energies correspond to the values at room temperature.

electron mass and high dielectric constant its Bohr radius of $a_{\mathrm{B}}^{*} = 10\,\mathrm{nm}$ (value in GaAs) is about two orders of magnitude larger. Another substantial difference is the possibility for electrons and holes to recombine by emitting a photon, leading to a finite lifetime of the quasiparticle. Due to the angular momentum of the photon, only transitions with $\Delta J = \pm 1$ are allowed and therefore the bright exciton has a total angular momentum of $J_{\mathrm{tot}} = \pm 1$. The angular-momentum-forbidden transitions with $\Delta J = \pm 2$ do not couple to light and contribute to the so-called "dark" states of the system.

Additionally to the optical and electrical properties, the possibility to combine different materials into heterostructures using molecular beam epitaxy (MBE) shows the true potential of III–V semiconductors. In this process, the bare elements get vaporized and then condense on a seed crystal, forming the crystalline structure layer by layer. This allows the combination of different elements while retaining a high purity of the sample. By growing a thin layer of a material with a smaller band gap we can break translational symmetry for the motion of the electrons and holes along the growth direction, effectively creating a 2D confinement called quantum well (QW). This results in an increased electron–hole binding energy and oscillator strength

[61]. For a QW larger than the Bohr radius, the confinement energy for the electrons and holes is given by:

$$E = \frac{\hbar^2 \pi^2}{2m^* d^2}, \tag{2.1}$$

with $m^* = m_\mathrm{e} + m_\mathrm{h}$ being the total mass of the exciton and d the thickness of the quantum well. The arising mass term splits the energies between the heavy hole and the light hole, reducing the degeneracy of the exciton ground state [62, 63]. Even though for III-V semiconductor QWs the thickness is usually comparable to the Bohr radius, the mass dependence and thus the splitting between the light and heavy hole remains.

This freedom in designing the sample structure also allows us to create more complicated excitonic structures. Growing a second QW separated by a thin barrier allows for the exchange of electrons and holes, leading to a spatial separation of the charges, forming the so-called indirect excitons (ix) [64] (Fig. 2.3 **a**). While on one hand the vanishing overlap between electron and hole reduces their light–matter coupling, their inherent dipole moment has proven to be a promising way to increase interactions in the system both theoretically [65, 66] and experimentally [44].

To describe the exciton system we use second quantisation with bosonic operators for the direct ($x^\dagger$) and indirect exciton ($y^\dagger$) which create excitons from the Fermi sea. Taking into account the in-plane momentum $\vec{k}$ and the two spin states (σ), the Hamiltonian of the system can be written as [65, 67]

$$\begin{aligned} H_\mathrm{ex} = \iint \frac{d^2\vec{k}}{(2\pi)^2} \sum_\sigma & E_\mathrm{dx}(\vec{k}) x_\sigma^\dagger(\vec{k}) x_\sigma(\vec{k}) + E_\mathrm{ix}(\vec{k}) y_\sigma^\dagger(\vec{k}) y_\sigma(\vec{k}) \\ & + \frac{J}{2}\left(x_\sigma^\dagger(\vec{k}) y_\sigma(\vec{k}) + y_\sigma^\dagger(\vec{k}) x_\sigma(\vec{k})\right), \end{aligned} \tag{2.2}$$

where J describes the tunnel coupling. By including the dc Stark effect and the dipolar energy shift in an external electric field, the energies of the

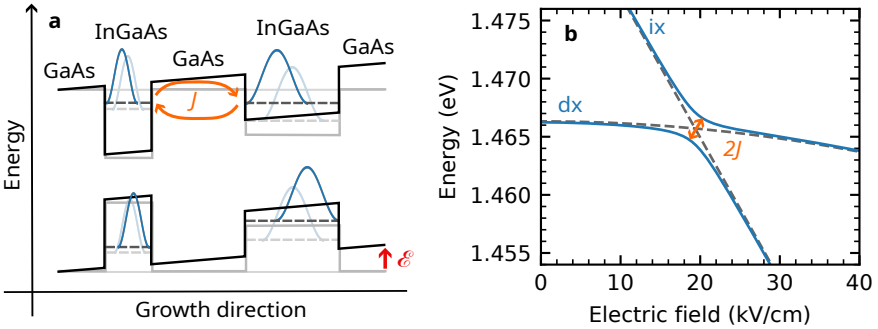

Figure 2.3: a Sketch of the conduction and valence band energy along the growth direction of the sample, showing the InGaAs QW pair embedded in the GaAs substrate with the corresponding energy levels. Applying an electric field shifts the energy levels, allowing the electrons to tunnel. **b** Energy shift of the direct (dx) and indirect exciton (ix) as a function of electric field. Due to the strong tunnel coupling, they hybridise on resonance, thereby forming an upper and lower exciton branch.

excitons close to $\vec{k} = 0$ are given by:

$$\begin{aligned} E_{\mathrm{dx}}(\vec{k}) &= E_{\mathrm{dx},0} + \frac{\hbar^2 \vec{k}^2}{2m_{\mathrm{dx}}} + \alpha \mathcal{E}^2, \\ E_{\mathrm{ix}}(\vec{k}) &= E_{\mathrm{ix},0} + \frac{\hbar^2 \vec{k}^2}{2m_{\mathrm{ix}}} + ed\mathcal{E}, \end{aligned} \tag{2.3}$$

where α describes the polarizability of the direct exciton, $\mathcal{E}$ the static out-of-plane electric field at the location of the QW, e the electric charge and d the dipole moment of the indirect exciton. We can use the electric field dependence to tune the exciton energies into resonance, shown in Fig. 2.3 **b**, where we plot the solution to H_{ex} at $k = 0$. Due to the tunnel coupling, the excitons hybridize close to resonance, leading to the shown anticrossing. The new eigenstates are superpositions of the direct and indirect exciton and inherit a fraction of both of their properties, leading to states with dipolar nature and a finite coupling to optical photons. To prevent a staggered arrangement of the dipoles occurring in a symmetric QW pair, an asymmetry

in the potential depth (see Fig. 2.3 **a**) can be introduced which only allows the tunneling of either electrons or holes at a given electric field.

2.2 Cavity photons

The basic idea of optical cavities is the formation of an electromagnetic standing wave between two mirrors due to constructive interference of the reflected photons. For the simplest case of two parallel mirrors, the constructive interference is perfect if the distance L between the mirrors is equal to a multiple of half the wavelength, leading to the mode energies

$$E_q = \frac{hcq}{2L}, \tag{2.4}$$

with q enumerating the different modes. The quality of an optical resonator is commonly described by its finesse $\mathcal{F}$, which quantifies the number of reflections of a photon inside the cavity until it leaks out through one of the mirrors [68],

$$\mathcal{F} = \frac{\pi}{|\ln(\sqrt{R_1 R_2} V)|} = \frac{\Delta E_\mathrm{c}}{\gamma_\mathrm{c}}, \tag{2.5}$$

and depends on the reflectivities R_1 and R_2 of the mirrors and the absorption per roundtrip V within the cavity. The finesse ultimately describes the separation of the resonances (free spectral range ΔE_c) relative to the cavity linewidth γ_c. Since the photon lifetime quantifies the loss of coherence from the cavity resonance, it defines a strong limit on observing phenomena which rely on the coherent exchange between states. Therefore to achieve strong coupling, the lifetime has to be longer than the coupling timescales between emitter and cavity and to be able to resolve the effects of interactions it has to be at least comparable to the scattering timescales. The photon lifetime τ_c and hence the linewidth are closely related to the finesse,

$$\tau_\mathrm{c} = \frac{1}{2\pi\gamma_\mathrm{c}} = \frac{\mathcal{F}L}{2\pi\hbar c}, \tag{2.6}$$

and additionally depend on the cavity length L.

Cavities with long lifetimes can therefore be achieved by using high-

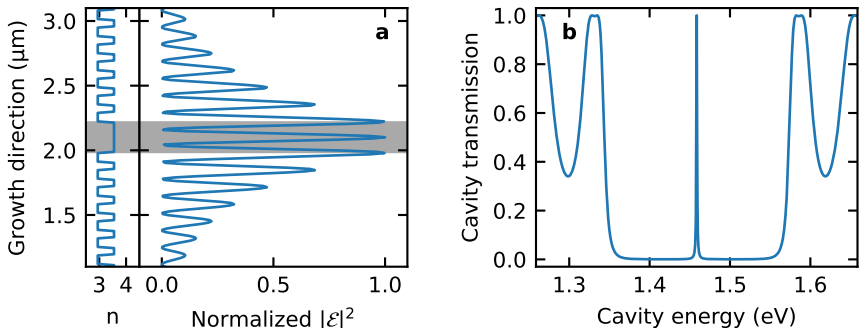

Figure 2.4: a Electric field inside a monolithic $\lambda/2$ cavity as commonly used in semiconductor structures calculated by the transfer matrix method (tmm). Here with 15 GaAs/AlAs DBR layers indicated by the refractive index of the materials as function on the growth direction shown on the left. **b** The transmission through the same cavity shows the stop band where both mirrors are highly reflective and a sharp resonance in the center.

reflectivity mirrors and by minimizing losses inside the mode volume. The best mirrors for this purpose are so-called distributed Bragg reflector (DBR) mirrors, where the thicknesses of two materials with different refractive indices are chosen such that the reflections from different interfaces destructively interfere with each other. By stacking multiple pairs on top of each other, reflectivities close to 100 % can be achieved. The reflectivity of such a mirror can be estimated using [69]:

$$R = \left[\frac{n_0 \left(n_2\right)^{2N} - n_\mathrm{S} \left(n_1\right)^{2N}}{n_0 \left(n_2\right)^{2N} + n_\mathrm{S} \left(n_1\right)^{2N}} \right]^2, \tag{2.7}$$

where n_1/n_2 are the refractive indices of the two materials, n_S/n_0 of the surrounding materials and N is the number of pairs. The downside of distributed Bragg reflector (DBR) mirrors is that it takes multiple layers to reach high reflectivities, allowing the electromagnetic field to penetrate into the mirrors, effectively increasing the cavity mode volume V_m

$$V_\mathrm{m} = \frac{\int d^3 r \varepsilon(\vec{r}) |\mathcal{E}(\vec{r})|^2}{\max |\mathcal{E}(\vec{r})|^2}, \tag{2.8}$$

where ε is the dielectric function. The penetration depth can be calculated using [70]

$$L_{\mathrm{DBR}} = \frac{\lambda_0}{4}\frac{1}{n_1 - n_2}, \tag{2.9}$$

where λ_0 is the design wavelength. In Fig. 2.4 we show the electric field inside a monolithic $\lambda/2$ cavity as commonly used in semiconductor structures, here calculated with 15 pairs of GaAs/AlAs DBR layers using the transfer matrix method[1] [72]. It nicely illustrates the penetration of the electromagnetic field inside the mirrors.

As we described before, we aim to enhance the interactions in our system by introducing an optical confinement via a hemispherical cavity, which essentially increases the mode overlap between the wave functions. The electromagnetic field inside a hemispherical cavity is described by Hermite–Gauss functions[2] where the different modes are labeled by integer numbers q for the longitudinal and (n, m) for the transverse electromagnetic modes (TEM). The energy of these cavity modes is given by [73]

$$\begin{aligned} E_{\mathrm{c}}^{q,m,n} = \frac{hc}{2L}\Bigg(&2\pi q + (2m+1)\arccos\sqrt{1-\frac{L}{r_x}} \\ &+(2n+1)\arccos\sqrt{1-\frac{L}{r_y}} + \Phi(E^{q,m,n})\Bigg), \end{aligned} \tag{2.10}$$

where r_x/r_y are the radii of curvature of the spherical mirror and Φ is an additional phase factor arising due to the penetration into the DBRs.

For the remainder of this thesis we focus on the cavity mode with the lowest momentum $n = m = 0$, as they are expected to have the longest lifetime. Similar to Eq. (2.2) we can describe the cavity photons using second quantisation by introducing the photon annihilation (a) and creation ($a^\dagger$) operators,

$$H_{\mathrm{c}} = \iint \frac{d^2\vec{k}}{(2\pi)^2}\sum_\sigma E_{\mathrm{c}}^{q,\sigma}(\vec{k}) a_{q,\sigma}^\dagger(\vec{k}) a_{q,\sigma}(\vec{k}), \tag{2.11}$$

[1] For the calculation we use the python tmm package [71].

[2] For a perfectly symmetrical cavity the modes would be described by Laguerre–Gauss functions, but asymmetries in the spherical mirror or in the substrate will lift the degeneracy.

where the momentum dependence of $E_{\mathrm{c}}^{q,\sigma}$ is given by the Gaussian profile of the mode and σ is the circular polarisation of the photon.

2.3 Exciton–polaritons

2.3.1 Light–matter coupling

Placing the semiconductor QW inside an optical cavity resonant with the excitonic transition allows for excitation and decay into the same photonic mode, thereby coherently coupling these different systems and combining their unique properties. The corresponding coupling strength is given by [74]

$$\Omega = \sqrt{\frac{4\pi E_{\mathrm{c}}}{\hbar L_{\mathrm{eff}}} f_{\mathrm{2D}}} \left| \frac{\mathcal{E}(z_{\mathrm{QW}})}{\mathcal{E}_{\mathrm{max}}} \right| \tag{2.12}$$

and depends on the relative electric field strength at the position z_{QW} of the QW, the effective length L_{eff} of the cavity taking into account the penetration into the DBRs, and the oscillator strength f_{2D} of the emitter describing the transition of the electron between the valence and conduction band. Using Eqs. (2.2) and (2.11) we can write down the Hamiltonian for the coupled system,

$$\begin{aligned} H = \iint \frac{d^2\vec{k}}{(2\pi)^2} \sum_{\sigma} & E_{\mathrm{dx}}(\vec{k}) x_\sigma^\dagger(\vec{k}) x_\sigma(\vec{k}) + E_{\mathrm{ix}}(\vec{k}) y_\sigma^\dagger(\vec{k}) y_\sigma(\vec{k}) \\ & + E_{\mathrm{c}}^{q,\sigma}(\vec{k}) a_{q,\sigma}^\dagger(\vec{k}) a_{q,\sigma}(\vec{k}) + \Omega \left(x_\sigma^\dagger(\vec{k}) a_{q,\sigma}(\vec{k}) + a_{q,\sigma}^\dagger(\vec{k}) x_\sigma(\vec{k}) \right) \\ & + \frac{J}{2} \left(x_\sigma^\dagger(\vec{k}) y_\sigma(\vec{k}) + y_\sigma^\dagger(\vec{k}) x_\sigma(\vec{k}) \right), \end{aligned} \tag{2.13}$$

where we assume the coupling of the cavity to the indirect exciton to be negligible due to the small overlap between electron and hole. In the current form the Hamiltonian is linear and can be diagonalized using a Bogoliubov transformation [13] by introducing the three new eigenstates

$$\begin{aligned} p_{i,\sigma}(\vec{k}) &= c_{\mathrm{c}}^i(\vec{k}) a_\sigma(\vec{k}) + c_{\mathrm{dx}}^i(\vec{k}) x_\sigma(\vec{k}) + c_{\mathrm{ix}}^i(\vec{k}) y_\sigma(\vec{k}) \\ i &\in \{\mathrm{LP}, \mathrm{MP}, \mathrm{UP}\} \end{aligned} \tag{2.14}$$

called the lower, middle and upper polaritons, which are superpositions of the cavity, the direct and the indirect exciton. The new eigenenergies at $\vec{k} = 0$ as a function of the photon energy are shown in Figs. 2.5 **b** and 2.5 **c** for different electric field strengths. For zero electric field, the direct and indirect excitons are detuned (Fig. 2.5 **a**) and only the direct exciton hybridises with the cavity photon, resulting in a single anticrossing. On the other hand, if the direct and indirect exciton are on resonance the cavity photons couple to a mixture of the two exciton states, resulting in two distinct anticrossings. Therefore, by changing the cavity energy and the electric field the composition of the polariton states can be tuned. This is quantified by the so-called Hopfield coefficients c_j^i which describe the composition of the polariton at a given energy and momentum in terms of its constituents. In the new diagonal form the Hamiltonian simplifies to

$$H = \iint \frac{d^2\vec{k}}{(2\pi)^2} \sum_{\sigma,i} E_i(\vec{k}) p^\dagger_{i,\sigma}(\vec{k}) p^i_{i,\sigma}(\vec{k}). \tag{2.15}$$

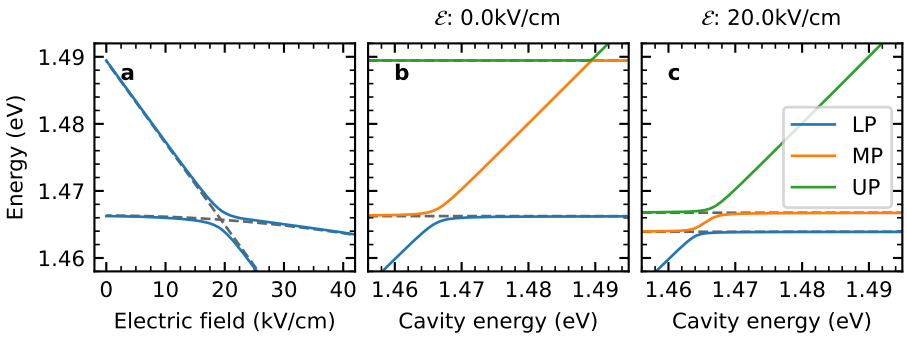

Figure 2.5: **a** Exciton energies as function of the electric field and (**b**, **c**) polariton spectra as function of the cavity energy for different electric fields. For $\mathcal{E} = 0\,\mathrm{kV/cm}$ the indirect exciton has no oscillator strength and the cavity couples only to the direct exciton, leading to one anticrossing shown in **b**. On the other hand at $\mathcal{E} = 20\,\mathrm{kV/cm}$, the direct and indirect exciton are hybridised, leading to three polariton states shown in **c**, which are a superposition of photon, direct and indirect exciton.

So far we assumed the ideal case of circularly polarised photons and exci-

tons. In reality the birefringence of GaAs leads to linearly polarised cavity modes which couple to a superposition of left and right circular polarised excitons. Since the middle and upper polariton can potentially decay into the lower polariton, their lifetimes are generally shorter. Therefore for the rest of this thesis we will focus only on the lower polariton branch. Additionally we will omit the momentum dependence, as we assume the excitation to populate the entire available k-space of the lowest momentum $m = n = 0$ mode. To simplify the notation we will therefore introduce $p^\dagger$ as the linearly polarised lower polariton creation operator.

2.3.2 Driven-dissipative polaritons

As the Hamiltonian we introduced in Eq. (2.15) is Hermitian it can only describe a closed system. For polaritons which couple to the environment through the cavity mirrors we therefore have to extend the model to include the decay and drive of the population. The creation of polaritons by an external laser can be described by adding a pump field with energy E_L. By moving to a frame rotating at the frequency of the drive the Hamiltonian becomes

$$H = -\Delta p^\dagger p + F^* p^\dagger + F p, \tag{2.16}$$

where $\Delta = E_\mathrm{L} - E_\mathrm{p}$ describes the detuning between the drive and the polariton and F is the excitation amplitude in the polariton basis.

To describe the dissipation of the system we use the so-called master equation in Lindblad form, a generalisation of the Schrödiger equation that includes coupling to a reservoir. By tracing out the reservoir the correlations are lost and the system becomes non-Hermitian. The dynamics for the density matrix of the system ρ are then described by [75]

$$\frac{\partial \rho}{\partial t} = \mathcal{L}\rho, \tag{2.17}$$

using the Liouvillian superoperator

$$\mathcal{L} = -\frac{i}{\hbar}\left[H, \rho\right] + \frac{\Gamma_\mathrm{p}}{2}\left(2p\rho p^\dagger - p^\dagger p\rho - \rho p^\dagger p\right) \tag{2.18}$$

in the limit of low temperatures where incoherent photon excitation can be

neglected. Here we have introduced the polariton linewidth Γ_p quantifying the decay into the reservoir. The corresponding equation of motion for the polariton operator is given by

$$\frac{\partial p}{\partial t} = -\left(\frac{\Gamma_\mathrm{p}}{2} + i\Delta\right) p - F + f_\mathrm{p}(t), \tag{2.19}$$

where $f_\mathrm{p}(t)$ is a operator describing the noise. Solving for the steady-state solution of the polariton density $n_\mathrm{p} = \left\langle p^\dagger p \right\rangle$, results in a Lorentzian line shape

$$n_\mathrm{p} = \frac{|F|^2}{\left(\frac{\Gamma_\mathrm{p}}{2}\right)^2 + \Delta^2}, \tag{2.20}$$

with a full width at half maximum (FWHM) of Γ_p.

2.3.3 Polariton lifetime

In the case of a single emitter coupled to an optical cavity, the polariton lifetime is simply given by the decay of the cavity through outcoupling or losses and the non-radiative decay of the emitter[3] scaled by their respective Hopfield coefficients. In reality the system is more complex, as small variations in the QW thickness lead to inhomogeneous broadening of the exciton energies and therefore to dephasing of their coherence. The coupling of the cavity to an inhomogeneous ensemble of emitters has been modeled and analyzed in [76] and we show in Fig. 2.6 **a** the resulting transmission spectrum. Due to the stochastic nature of the thickness fluctuations we assume a Gaussian distribution of emitters. Assuming the width of the inhomogeneous distribution to be smaller than the light–matter coupling strength $\Omega > \gamma_\mathrm{inhom}$, the model provides an approximation of the polariton linewidth by evaluating the poles of the transmission function to first order at the energies $E_\mathrm{x} \pm \Omega$:

$$\Gamma_\mathrm{p} = \frac{1}{2}\left(\gamma_\mathrm{c} + \gamma_\mathrm{x} + 2\pi\rho(E_\mathrm{L})\Omega^2\right). \tag{2.21}$$

[3] Note that the radiative decay of the emitter does not contribute, as it is part of the light–matter coupling mechanism.

Here, γ_x describes the non–radiative decay of the exciton and the function ρ the energy distribution of the emitters which is evaluated at $E_L = E_x \pm \Omega$. For a Gaussian distribution, ρ decays faster than $(E_L - E_x)^{-2}$ and the last term vanishes at the polariton resonances around $E_L = E_x \pm \Omega$. In other words, due to the strong light–matter coupling, the polariton resonance is far detuned from the inhomogeneously broadened emitters, essentially only coupling to a narrow band of excitons. This "cavity protection" is valid as long as the polariton energy is sufficiently far detuned from the inhomogeneously broadened exciton ensemble, and allows for polariton linewidths which are significantly narrower than the bare cavity or exciton linewidths as shown in Fig. 2.6 **b**.

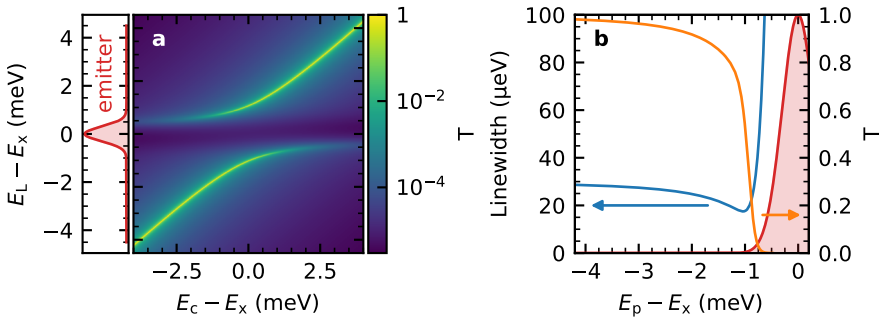

Figure 2.6: **a** Polariton spectrum as a function of cavity–exciton detuning for a cavity coupled to inhomogeneously broadened emitters with Gaussian distribution ($\gamma_{inhom} = 0.6\,$meV FWHM), indicated on the left of the figure. **b** The linewidth (blue) and peak transmission (orange) of the lower polariton as function of the polariton–exciton detuning. While the linewidth initially drops with the reduced cavity content, it immediately increases by an order of magnitude as the polariton energy approaches the inhomogeneous exciton distribution (red).

2.4 Polariton interactions

One of the major strengths of polaritons is the combination of attributes from two substantially different particles, which allows us to engineer photonic states which inherit the interactions from the excitons. Due to their

charged constituents, excitons exhibit Coulomb interactions, which for low kinetic energies ($|k| < 1/a_\mathrm{B}$), where the scattering event does not resolve the excitonic substructure, can be described as a contact potential [77]. Due to its symmetry the scattering process conserves the spin of the exciton and we can distinguish between same-spin (triplet) and opposite-spin (singlet) interactions. While in general the singlet interactions are negligible, they can couple to the biexciton bound state which acts as a Feshbach resonance and significantly increases the singlet interaction strength [41, 42]. But since we expect the triplet interactions to be dominant in our system, we will limit our description to them for the rest of this work. For the rest of the description we will focus on the triplet interactions, as we expect them to be dominant in our system.

In the polariton basis we can write the corresponding interaction Hamiltonian

$$H_\mathrm{int} = \frac{g_\mathrm{pp}}{2} p^\dagger p^\dagger p p, \tag{2.22}$$

where $g_\mathrm{pp} = U_\mathrm{pp}/A$ is the polariton interaction strength per area A and the factor of 2 in the denominator accounts for the admixture of left and right circularly polarized excitons. The effective interaction strength for polaritons is calculated by evaluating the expectation values of $\langle \Phi_i | H_\mathrm{int} | \Phi_j \rangle$ for interactions between direct excitons, indirect excitons and between direct and indirect excitons [65]. Using the Born approximation, the polariton interaction strength is simply the sum of the three interaction processes scaled by their respective Hopfield coefficients,

$$U_\mathrm{pp} = |c_\mathrm{dx}|^4 U_\mathrm{dxdx} + |c_\mathrm{ix}|^4 U_\mathrm{ixix} + |c_\mathrm{dx}|^2 |c_\mathrm{ix}|^2 U_\mathrm{dxix}, \tag{2.23}$$

with the following expressions for the different interaction strengths:

$$\begin{aligned} U_\mathrm{dxdx} &\simeq 6\varepsilon_\mathrm{x} a_\mathrm{B}^{*2}, \\ U_\mathrm{ixix} &\simeq \varepsilon_\mathrm{x} a_\mathrm{B}^2 \left(6 + 3.5 \frac{d}{a_\mathrm{B}}\right), \\ U_\mathrm{dxix} &\simeq \varepsilon_\mathrm{x} a_\mathrm{B}^2 \frac{1}{\frac{1}{6} + 1.2\frac{d}{a_\mathrm{B}}}, \end{aligned} \tag{2.24}$$

with the exciton binding energy ε_x, the Bohr radius a_B^* and the separation

between the QWs d. For GaAs we find $\varepsilon_\mathrm{x} = 10\,\mathrm{meV}$ and $a_\mathrm{B}^* = 10\,\mathrm{nm}$ resulting in an exciton interaction strength $U_\mathrm{dxdx} \approx 6\,\mu\mathrm{eV}\mu\mathrm{m}^2$, while for realistic parameters of the QW separation $d/a_\mathrm{B} \approx 1$ and therefore $U_\mathrm{ixix} \approx 1.6\,U_\mathrm{dxdx}$ and $U_\mathrm{dxix} \approx 0.12\,U_\mathrm{dxdx}$.

Measuring the polariton interaction strength has already been attempted in multiple experiments, which are summarized in Fig. 2.7 inspired by [78]. The spread of values over orders of magnitudes highlights the difficulty of obtaining consistent results. Most of the reported values relied on measuring the blueshift $\Delta E = g_\mathrm{pp} n_\mathrm{p}^2$ of a polariton condensate [46, 78–81], where the main difficulty lies in separating the energy shift obtained from polariton–polariton interactions from interactions with the exciton reservoir created by the strong drive or from a blueshift originating from strong confinement. Other experiments measured the interaction strength from the wave velocity $c = \sqrt{\hbar g_\mathrm{gg} n_\mathrm{p}/m}$ of excitations in a polariton fluid [16] or by observing the exact shape of propagating solitons in polaritons [82]. The last set of experiments [54, 55] measure non-classical correlations originating from the polariton interactions which we will discuss more in the next section.

Recent theoretical work [83] describing the interactions between indirect exciton–polaritons in 1D found a much stronger dependence of the polariton interactions on the detuning between exciton and polariton than described by the Hopfield argument in Eq. (2.23). They find that due to the ultra-light mass inherited from the photonic content, the energy cost of two polaritons avoiding their spatial overlap is high and the resulting increased polariton interaction energy can exceed the one between bare excitons. While the theory was developed for 1D indirect exciton–polaritons, it could be expected that the argument also holds for 2D and direct excitons and that therefor Eq. (2.23) might not describe the system accurately.

2.4.1 Polariton blockade

Since the polariton interaction strength is orders of magnitudes smaller than the light–matter coupling $U_\mathrm{pp} \ll \Omega$, the polariton basis p remains a good description of the system. The Hamiltonian H_int can therefore be treated as a perturbation of the polariton spectrum and results in an energy shift

$$\Delta E = \frac{g_\mathrm{pp}}{2} \left(n_\mathrm{p} - 1\right)^2 \tag{2.25}$$

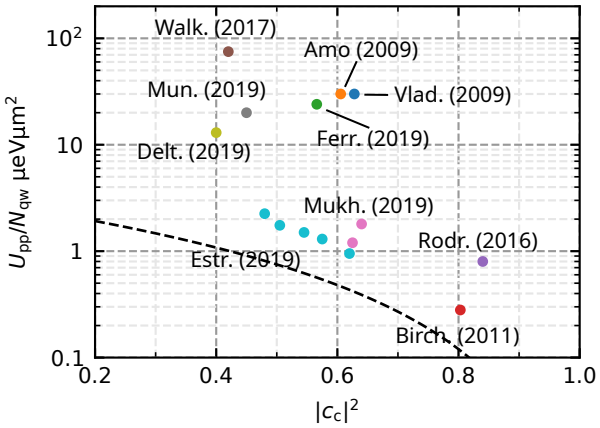

Figure 2.7: Overview of different experimentally obtained values for the polariton interaction strength normalized by the number of QWs found in the literature. It shows a spread of the observed values over orders of magnitudes, highlighting the difficulty of obtaining an accurate number for the interaction strength. The black line corresponds to Eq. (2.23) with $|c_{ix}|^2 = 0$ and $U_{xx} \simeq 6\,\mu\text{eV}\mu\text{m}^2$. The figure is adapted from [78] and the experiments are described in [16, 46, 54, 55, 78–82].

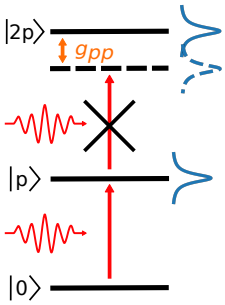

Figure 2.8: Illustration of the polariton blockade. If the polariton interaction is larger than the linewidth, the second state of the polariton manifold $|2\rangle$ experiences a blueshift $g_{\mathrm{pp}}/2$. Therefore photons which are resonant with the $|0\rangle \rightarrow |1\rangle$ transition do not carry enough energy to excite the $|2\rangle$ state.

proportional to the number of polaritons in the system. As a result, the originally harmonic polariton excitation ladder becomes anharmonic as the states with $n_{\mathrm{p}} > 1$ experience a blueshift, as illustrated in Fig. 2.8. In the ideal case of a blueshift larger than the linewidth, the system enters the blockade regime [25] where, analogous to a 2-level system, the absorption of a first photon blocks subsequent excitations as the only available state is already occupied. The photons emitted from this transition are therefore perfect single-photon Fock states, which are an essential building block for quantum information and cryptography protocols [5, 6].

In reality we expect the interaction strength to be smaller, but still comparable to the linewidth. In this scenario, we can still observe a reduced blockade if we excite the polariton slightly red detuned from the resonance. Depending on the blueshift and the actual laser detuning, the polariton manifold gets truncated at a maximal occupation number thereby leading to a superposition of Fock states. This new state is not an eigenstate of the Fock basis and therefore shows finite number fluctuations, but since the manifold is truncated the fluctuations are reduced and the new state still shows sub-Poissonian statistics. If one additionally suppresses the excitation of the higher occupation numbers in the Poissonian distribution by using a weak drive, the output of such a system can be a good approximation for a single-photon state, even if it is not in the strongly interacting regime.

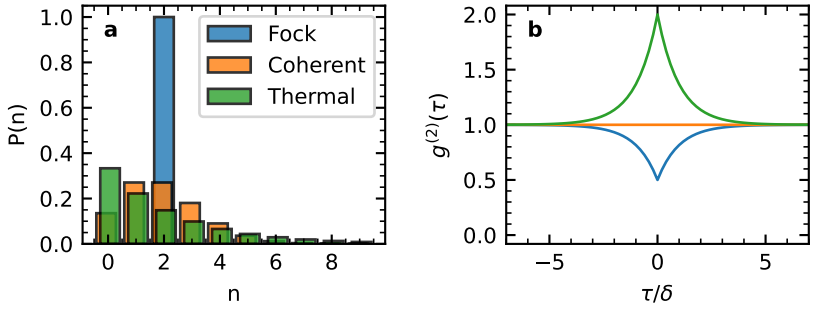

Figure 2.9: a Photon number distribution and **b** second-order correlation function for a Fock, coherent and thermal state each with a photon number expectation value of 2. For a coherent state the photons are uncorrelated and follow Poissonian statistics with a constant value of $g^{(2)}(\tau) = 1$. Photons from a thermal source are strongly correlated, leading to super-Poissonian statistics and a bunching peak. On the other hand, a Fock state has no number fluctuations, leading to sub-Poissonian statistics and a characteristic antibunching dip. The time axis is normalized by the time scale δ, which depends on the nature of the physical process.

2.4.2 Second-order correlations

The single-particle nature of photons can be distinguished from coherent or thermal light by its statistical distribution. Depending on the nature of fluctuations in a system the occupation probability $P(n)$ changes, as shown in Fig. 2.9 **a**. For a coherent state the fluctuations are entirely uncorrelated and therefore follow a Poissonian probability distribution with a variance $\langle \Delta n^2 \rangle = \langle n \rangle$. For a thermal state the fluctuations are strongly correlated, for example by stimulated emission, and the distribution decays exponentially with a larger variance (super-Poissonian statistics) $\langle \Delta n^2 \rangle = \langle n \rangle^2 + \langle n \rangle$. On the other hand, a Fock state has a single-valued occupation probability $P(n) = \delta(n)$, there are no fluctuations (sub-Poissonian statistics) and the variance is therefore $\langle \Delta n^2 \rangle = 0$.

This statistical property is quantified by the second-order (or intensity) correlation function which in the notation of second quantisation is given by

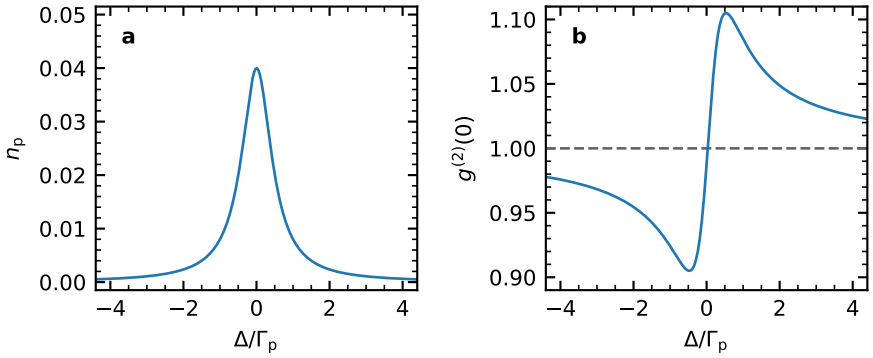

Figure 2.10: Numerical solution to Eq. (2.17) and Eq. (3.1) for a weak drive and $g_{pp}/\Gamma_p = 0.1$. It shows the expected Lorentzian line shape of n_p and a "S" shape for $g^{(2)}(0)$. While for negative detunings the photon energy is insufficient to excite the $|2\rangle$ state, resulting in antibunching, for positive detunings it becomes resonant leading to a bunching signature.

[84]

$$g^{(2)}(t,\tau) = \frac{\left\langle a^\dagger(t)a^\dagger(\tau)a(\tau)a(t)\right\rangle}{\langle a^\dagger(t)a(t)\rangle \langle a^\dagger(\tau)a(\tau)\rangle}. \tag{2.26}$$

It describes the probability of observing a photon at time $\tau = t + \Delta t$ conditioned on the observation of a photon at time t. Since for our purposes the time at which the first photon was detected is irrelevant, we will omit t and write $g^{(2)}(\tau)$ for the rest of this thesis. In Fig. 2.9 **b** we show $g^{(2)}(\tau)$ for the cases of a Fock, coherent and thermal state. For coherent light it is equally probable to detect photons at any time and therefore $g^{(2)}(\tau) = 1$, for thermal light there is a higher probability to observe multiple photons at the same time leading to a bunching peak and a Fock state has a reduced probability of observing multiple photons at the same time, leading to an antibunching dip. This observation is a benchmark for quantum states, as it can be shown that for classical states $g^{(2)}(0) \geq 1$ and $g^{(2)}(0) \geq g^{(2)}(\tau)$.

By numerically solving the master equation Eq. (2.17) (for more details on the simulations see A) and then calculating Eq. (2.26) we obtain the polariton density and $g^{(2)}(0)$ as function of the laser detuning, as shown in Fig. 2.10 for a weak drive and $g_{pp}/\Gamma_p = 0.1$. Fig. 2.10 **b** shows a "S" shaped dependence

of $g^{(2)}(0)$ on the laser detuning which can be intuitively understood using the blockade picture in Fig. 2.8. For negative detunings the photons have insufficient energy to excite the $|2\rangle$ polariton state leading to antibunching, while for positive detunings the photons are resonant, resulting in bunching. In the limit of low densities and weak interactions, the minimum of $g^{(2)}(0)$ as a function of detuning follows [25, 85]

$$\min\left(g^{(2)}(0)\right) = 1 - \frac{U_{\mathrm{pp}}}{A\Gamma_{\mathrm{p}}}. \tag{2.27}$$

This simple expression sets the benchmark for observing strong correlations in a polariton system, where the interaction strength per area has to overcome the width of the polaritons, which is already illustrated by the blockade picture shown in Fig. 2.8.

Chapter 3

Experimental methods

In this chapter we introduce the experimental foundations necessary to measure correlations of exciton–polaritons. First we describe the gated semiconductor QW structure and the hemispherical fiber cavity allowing us the excitation of confined exciton–polaritons and the control over their composite nature. Then we describe the experimental setup, including cryogenics, optical excitation and detection. And finally we spectroscopically characterize the polaritons that are created in our system to be able to understand and control their properties.

3.1 Sample and fiber cavity

The formation of polaritons with their hybrid exciton–photon nature requires two major ingredients, a semiconductor matrix which can host optical excitations, e.g. excitons, and an optical cavity that provides a long-lived photon field. In our experiment, the excitons are excited in a III–V semiconductor QW which is grown on top of a flat mirror structure forming one of the cavity mirrors as illustrated in Fig. 3.1. The second mirror is fabricated on the curved facet of an optical fiber. The resulting cavity mode features a reduced lateral size leading to a spatial confinement of the generated polaritons thereby enhancing the polariton–polariton interaction strength. The design of such an open microcavity allows for a change of cavity length over

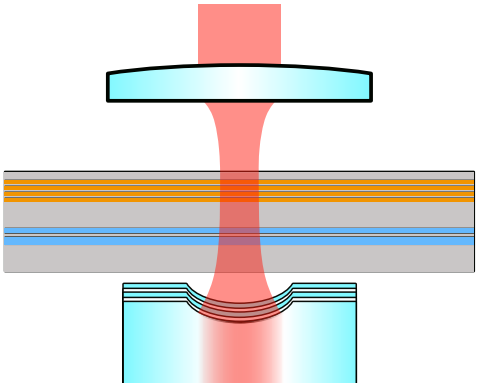

Figure 3.1: Sketch of the hemispherical cavity formed by the curved fiber surface and the DBR in the GaAs substrate hosting the InGaAs QW pair. Photons can be injected and extracted into the mode via the fiber or a collimating lens.

a wide range and offers full control of the detuning between the optical resonance and the exciton energy. Mounting the sample over a hole allows us to not only inject and extract photons directly through the fiber containing the cavity mirror, but also through free space via the polished back side of the sample. This makes it possible to measure the reflection or the transmission from both sides, with transmission being the more favorable configuration, as it allows to only observe photons originating from the cavity.

3.1.1 Sample

To get to the regime where the interactions are comparable to the loss rates in the system, we require a sample with high quality photonic and excitonic properties. Therefore the uniformity of the QW and the substrate DBR, which influence the linewidth of the exciton and of the cavity mode, are crucial. To achieve this high quality, the samples were grown using MBE by Dr. Stefan Fält at the "Advanced Semiconductor Quantum Materials" group led by Prof. Werner Wegscheider at ETH Zürich. At the heart of the sample, shown in Fig. 3.2 **a**, lies the InGaAs QW pair, hosting the excitons. It is made up of a thin (4.5 nm) and a thick (10 nm) layer of InGaAs with an estimated indium content of about 6 %, separated by a 12 nm tunnel barrier made from GaAs which is placed at an antinode of the intracavity field.

The asymmetry in the thicknesses leads to an offset in the electron and hole energies between both QWs. Consequently the electron levels in both QWs can be brought into resonance by applying an electric field, while the holes remain detuned. Therefore only the negative charges can tunnel between the QWs, leading to the desired dipolar character of the indirect excitons. To apply an electric field and tune the energy of the charged particles, an electron-doped layer (Si doping with a nominal density of $4 \cdot 10^{18}\,\mathrm{cm}^{-3}$) and an hole-doped layer (C doping with a nominal density of $1 \cdot 10^{18}\,\mathrm{cm}^{-3}$) are grown surrounding the QW pair, thereby forming a p–i–n structure. They are placed in respective nodes of the cavity field to reduce their overlap with the optical modes thereby reducing their effective absorbance. To prevent the charges from tunneling between these different layers, additional AlGaAs layers are grown between the doped layers and the QW pair, whic acts as a tunnel barrier due to the larger band gap.

The second part of the sample is one of the two DBR mirrors forming the optical cavity. In our samples the DBR is designed for a centre wavelength of 850 nm formed by 24 layers of GaAs and 25 layers of AlAs, with refractive indices of $n_{\mathrm{GaAs}} = 3.55$ and $n_{\mathrm{AlAs}} = 2.94$. To estimate the reflectivity of the mirror we use Eq. (2.7) resulting in $R = 99.992\,\%$. To increase the reflectivity, one would ideally increase the number of pairs. However, since there is a lattice mismatch between GaAs and AlAs, growing more layers can lead to an accumulation of tension within the structure which is released by forming line defects. The chosen number of DBR layers is a compromise between reflectivity and sample quality.

The full structure is grown on a wafer from which a suitable piece of about $5\,\mathrm{mm} \times 5\,\mathrm{mm}$ is selected and cleaved. To make contacts to the doped layers of the sample we deposit gold pads on each side as shown in Fig. 3.2 **b** on the right. Since the n-doped layer (Fig. 3.2 **a**) is below the p-doped one, we use photolithography and wet etching to remove the p-layer and then deposit the gold pad in the trench. The gold pads are then connected via wire bonding to leads on the sample holder which allow for an electrical connection. Due to the macroscopic structure of the etched contacts, we later simplified the procedure by replacing the photolithography step by a manually removing the photoresist with aceton. Then the contacts can be soldered directly by hand using indium and an annealing step for the n-doped layer and indium with 4 % zinc for the p-doped layer.

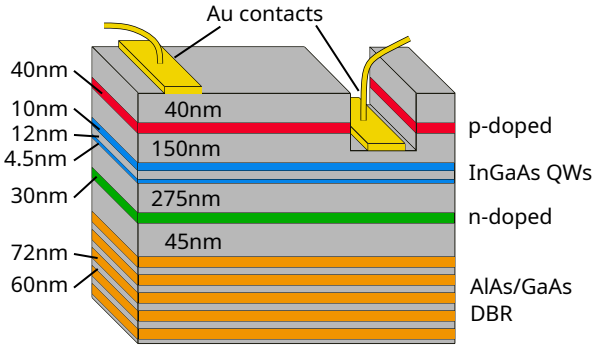

Figure 3.2: Schematic of the sample structure. On the bottom are 25/24 layers of AlAs/GaAs forming the DBR of one of the cavity mirrors. Grown on top is the asymmetric InGaAs QW pair surrounded by the p- and n-doped layers. The contact to the p-doped layer is fabricated directly on the GaAs surface, while for the contact to the n-doped layer the substrate has been etched away until the p-doped layer is removed.

3.1.2 Fiber

The second mirror was fabricated on a partially curved fiber surface forming a hemispherical cavity together with the semiconductor mirror. The curved mirror leads to a lateral confinement of the optical mode where the area is smallest at the surface of the flat mirror. As the QW is placed close to the DBR inside the sample, the mode area is still close to its minimum, allowing us to excite polaritons in an area as small as possible by optical confinement.

The curved fiber surface was fabricated by laser ablation with a highly focused CO_2 laser, which resulted in the evaporation and partial melting of the glass, leaving behind a curved depression with low roughness on the surface of the fiber tip [53]. The surface is then coated with 18/17 pairs of a Ta_2O_5/SiO_2 DBR to form the mirror with an expected reflectivity of $R = 99.999\,96\,\%$. Due to the higher refractive index contrast between these two materials ($n_{Ta_2O_2} = 2.09$, $n_{SiO_2} = 1.47$) the resulting reflectivity is significantly higher than for the GaAs/AlAs DBR. The resulting asymmetry of reflectance leads to 98 % of the intracavity field leaking out through the semiconductor mirror, making it more efficient to detect photons from this

side of the cavity. The shape and position of the dimple was characterized using an interferometric measurement to ensure a clean shape and good overlap of the dimple with the fiber core. The specific fiber used in this thesis is the same as in the works [19] and [54] with a radius of curvature of 13.9 µm near the centre of the dimple. The most important number for this work is the area of the optical mode, as it determines the polariton–polariton interaction energy. It was measured by using a knife edge technique and for the fiber in this setup the beam diameter was measured to be 2.18 µm. A more in-depth description of the fabrication and characterisation can be found in [86].

3.2 Setup

3.2.1 Cryogenics

While it is possible to observe excitons at room temperature, the thermal fluctuations ($\approx 26\,\mathrm{meV}$) are larger than the coupling between excitons and photons. Additionally the excitons are substantially broadened due to the kinetic energy of the electrons and the high occupation of phonons. Therefore, to resolve the exciton–polariton spectrum and to achieve low linewidths, we cool the sample to about 4 K using a liquid helium bath cryostat which is sketched in Fig. 3.3. We use a 100 l liquid helium Dewar (CRYOFAB CMSH 100l, 6.35 cm neck diameter) capable of holding an insert containing the cryogenic cavity setup together with the sample. The sample itself is suspended over a hole in a titanium holder to gain optical access from free space. The holder is then mounted upside down on piezoelectric x/y-positioners, while the fiber, fixed on a holder mounted on a z-positioner and protruding by a few millimeters, is facing the sample from the bottom. The positioners can be used in two modes, a stepping motion which is used to cover distances of several millimeters and a linear motion with sub-micrometer resolution achieved by applying a static voltage to the piezoelectric element. The x/y-positioners (attocube ANPx101/RES/LT) allow us to explore different regions on the sample which is necessary, as imperfections in the doping layers of the sample lead to a drop in voltage away from the contact and also to be able to avoid deposits on the sample surface. The z-positioner (attocube ANPx101/RES/LT) on the other hand allows for tuning of the cavity length

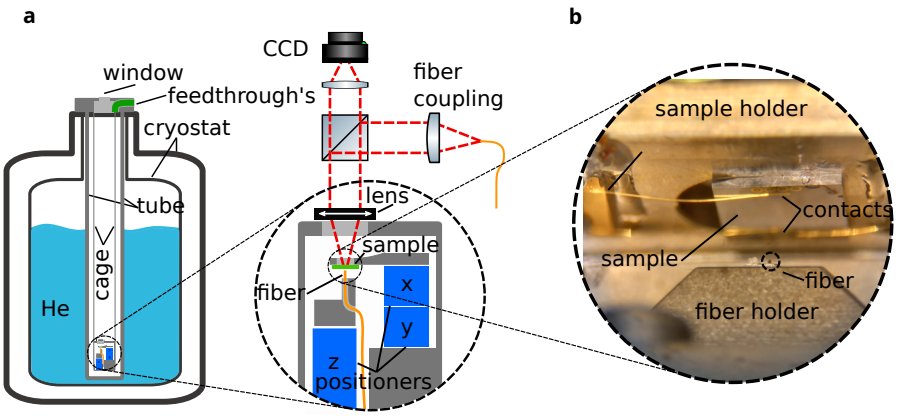

Figure 3.3: a Cryogenic measurement setup and **b** image of the sample mounted upside down above the fiber. On the left the He dewar used as a cryostat is sketched. The sample and the fiber are mounted inside a box (see close-up) which is suspended on rods inside a tube filled with 25 mbar He exchange gas. To adjust the cavity length, the fiber is mounted on a z-positioner, while the sample is mounted on x/y-positioners. A lens with focus on the sample together with a window on top of the tube and a fiber coupling setup with a camera for imaging allows for free space optical access to the sample. Electrical and fiber feedthroughs located on top of the tube allow to interact with the system when it is cooled down.

and thus bringing the cavity in resonance with the exciton. These elements are mounted together on a titanium chuck which itself is inside a tube submerged in liquid helium. To provide thermal contact between the sample and the walls of the tube, the air is evacuated and replaced with 25 mbar of helium serving as an exchange gas.

The insert is equipped with a number of vacuum feedthroughs for the transmission of optical and electrical signals. Furthermore, a free space optical access via a window on top of the insert is available, which together with a lens (Thorlabs A397tm-b) focused on the sample, allows to send and receive light from the other side. Hence, the setup allows for measurements not only in reflection but also in transmission. The electrical connections are used to control and read out the positioners and to apply a voltage generated by a source measure unit (Keithley 2400 source meter) to the p–i–n junction

on the sample.

3.2.2 Optical setup

The last key ingredient to perform the experiment is the optical setup, here divided into excitation, coupling to the cavity and detection. The setup is built in a way that all the different components for excitation and detection are fiber-coupled and can be easily exchanged. The main light source

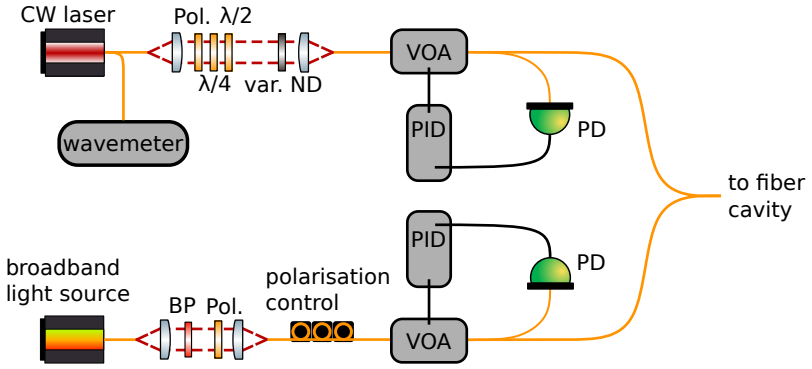

Figure 3.4: Setup for the excitation light sources. Both sources are power-stabilized by a VOA which is controlled by a proportional–integral–derivative controller (PID). For the polarisation control of the continuous wave (CW) laser a polarizer (Pol.) and a half- and quarter-wave plate are placed in the free space path, while for the broadband light source a polarizer and a fiber paddle are used. As the CW laser is used as energy reference for the experiment, a fraction of the light is sent to a wavemeter to obtain a precise readout of the wavelength. For the broadband light source we use an additional bandpass filter (BP) to absorb light outside of the stop band of the cavity mirrors.

is a CW diode laser (New Focus Velocity TLB-6316) which is tunable between 838 nm to 853 nm with a linewidth below 300 kHz. For alignment and quick characterizations a broadband light source (Thorlabs SLD8305-A10) centered around 830 nm is connected to the setup. Both light sources are fiber-coupled, polarization-controlled and power-stabilized before getting combined in a fiber beam splitter connected to the experiment, see Fig. 3.4. For the polarisation control of the CW laser, the light is first coupled to free

space where the polarisation is defined using a polarizer and then adjusted with a quarter- and a half-wave plate. To have some additional power control, a beam block and a wheel with variable neutral-density (ND) filter is installed before the light is coupled back into a fiber. For the broadband light source the setup is similar, with the difference that the wave plates are replaced with fiber polarization controllers after the light is re-coupled into the fiber. Additionally there is a removable bandpass filter (Thorlabs FB850-40) to block light outside of the stop band of the DBR mirrors. For the power stabilisation, a PID controller (Stanford Research Systems SIM960) is using the signal from a photo diode to control the attenuation of a variable optical attenuator (VOA) (Thorlabs V800A). To get the signal for the photo diode a part of the light is split off with a fiber beam splitter. As the CW laser is used to excite the polaritons and determine their energies, its wavelength sets the energy reference for the whole experiment. To have a precise readout of the wavelength, a fiber beam splitter is sending a portion of the light to a wavemeter (High Finesse WSU-30/661) which interferometrically determines the wavelength with an accuracy below 30 MHz.

As mentioned above, the cryogenic setup allows for two ways to couple light into the optical cavity. While on one side we can directly send light through the fiber with the cavity mirror, we also have free space optical access through the top window on the insert. To direct light through the window and the lens to the sample, a small cage system is mounted on top of the insert with a fiber coupler and an alignment system with the necessary degrees of freedom. It also contains a camera with which we are able to image the sample, inspect the shape of the cavity modes and to help with the alignment.

To analyse the optical signal from the sample we use three different detector setups: a correlation setup, detectors to measure transmitted intensity and a spectrometer together with a nitrogen-cooled camera. To resolve correlations of single photons on timescales on the order of 40 ps given by the polariton lifetime, we need single-photon detectors with a low timing uncertainty (jitter). Currently the detectors with the lowest timing resolution are superconducting nanowire single-photon detector (SSPD) (in our experiment detectors from Single Quantum, low jitter variant). This detector technology is based on superconducting nanowires cooled to 1.8 K with a closed-cycle cryostat (pulse tube refrigerator). A current close to the critical

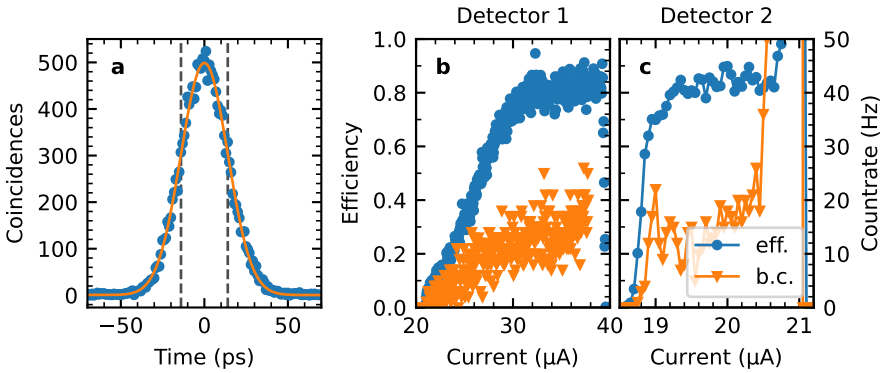

Figure 3.5: Characterisation of the superconducting nanowire single-photon detectors (SSPDs). **a** Autocorrelation of a 1 ps long laser pulse. The detected pulse width is prolonged by timing uncertainty of the detector and the correlation electronics and is extracted by a Gaussian fit (orange line) $\sigma_{\text{tot}} = 14\,\text{ps}$. Substracting the jitter of the electronics allows for an estimate of the average detector timing uncertainty of $\sigma_{\text{det}} = 4.9\,\text{ps}$. **b**, **c** Detector efficiency (eff.) and corresponding background counts (b.c.) as function of the driving current. The background is dominated by photons from the lab and the dark counts only appear shortly before the breakdown current, as can be seen for example on detector 2 at about 20.5 µA. The optimal working point is on the onset of the efficiency plateau.

current of the superconductor is flowing through the wires, such that if a photon is absorbed by the nanowire it becomes normally conducting thereby creating a voltage pulse. Since the wires have to recover superconductivity after detecting a photon, they have a dead time of several nanoseconds. To nonetheless detect two successive photons within this dead time, we use a Hanbury Brown and Twiss (HBT) setup, where we split the optical signal and send it to two detectors as shown in Fig. 3.6 **a**. The pulses from the detectors are then read out and analysed with time-correlated single photon counting (TCSPC) electronics (PicoQuant HydraHarp 400), which can either measure the time difference between pulses arriving on different channels or directly record the arrival times of the pulses in the form of time tags. Under optimal conditions, the efficiency of the detectors was measured to be 85 % while the background counts stemming from room light are on the order of twenty counts per second, see Fig. 3.5 **b** and Fig. 3.5 **c**. The actual dark

counts are smaller than the background light and only appear close the the critical current, as can be seen in Fig. 3.5 for detector 2 at about 20.5 µA. To estimate the timing jitter of the correlation system we measure the autocorrelation of a 1 ps long laser pulse shown in Fig. 3.5 **a**. The width of the signal is a sum of the different elements $\sigma^2_{\text{tot}} = \sigma^2_{\text{elect}} + 2\sigma^2_{\text{det}} + 2\sigma^2_{\text{pulse}}$ namely from the correlation electronics, detector jitter and the duration of the laser pulse. Fitting a Gaussian curve to the signal allows us to extract the total jitter of $\sigma_{\text{tot}} = 14\,\text{ps}$ and knowing the optical pulse length we can estimate the total jitter of the detection system to be $\sigma_{\text{sys}} = 13.9\,\text{ps}$. By using the timing uncertainty provided by the manufacturer of the correlation electronics we can also estimate the average jitter per detector to be$\sigma_{\text{det}} = 4.9\,\text{ps}$.

In a last characterisation step we also want to make sure that we do not detect correlated noise on the time scales of the expected polariton lifetime. To characterize this we send strongly attenuated light from the CW laser to the detectors and measure the correlations, shown in Fig. 3.6 **b**. In the blue trace are visible oscillations around $\tau = 0$, suggesting crosstalk between the two channels. This noise is centred around the zero time delay $\tau = 0$ defined by the correlation electronics. As we are interested in two photons arriving simultaneously on the beam splitter, we can separate the real zero time delay between photons from the electronic zero time delay in the detection by adding 5 m of additional optical fiber in one of the arms after the beam splitter. As a result, the pulses corresponding to two photons which arrive on the beam splitter at the same time arrive on the correlation electronics shifted by 23 ns. The corresponding correlations are shown in Fig. 3.6 **b** in orange which we inspect closer in Fig. 3.6 **c** where we show the standard deviation calculated for bins of 100 coincidences. While below 10 ns there are still some remaining oscillations leading to enhanced fluctuations, the standard deviation approaches quickly the value associated with the shot noise.

The second detector setup is a pair of Si based avalanche photodiodes (APDs) (EXCELITAS SPCM-AQRH-14 and EXCELITAS SPCM-AQRH-16) which are a different type of single-photon detectors with much larger jitter (350 ps) than the SSPDs. Due to their simpler construction and connection to the setup they are more convenient to measure the photon countrate. Since the APDs saturate and behave sub-linearly at countrates above approximately 2 MHz, it is practical to split the signal and send it to two detectors,

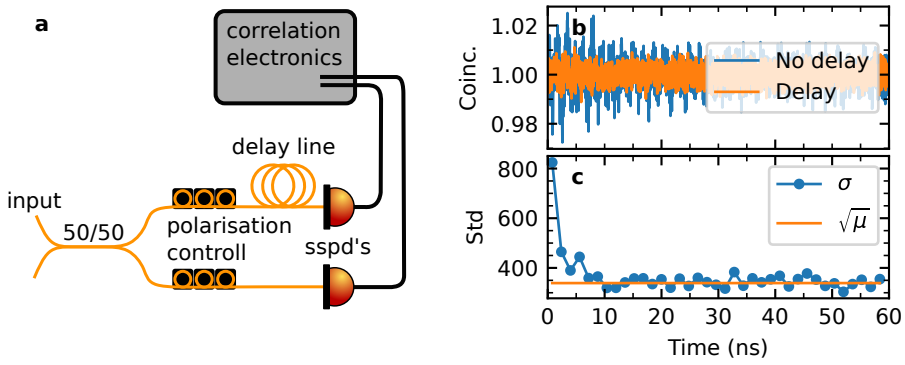

Figure 3.6: **a** HBT setup with detectors and correlation electronics. The light coming from the sample is split with a fiber beam splitter and then sent to the two detectors. The arrival times of the electrical pulses from the two detectors are analysed with TCSPC correlation electronics. A length of 5 m of additional fiber in one arm separates the electronic zero time delay by 23 ns from the optical one, which is defined by two photons arriving at the beam splitter. **b** Correlations of a CW laser with and without delay line. Adding the delay line moves the oscillations seen in the first 10 ns of the blue trace to negative delays such that they are not visible in the orange trace. **c** Standard deviation of bins of 100 coincidences measured with delay line shown in **b**. While there are still some remaining oscillations, standard deviation quickly approaches the shot noise limit after about 10 ns.

effectively doubling the linear regime. This provides enough dynamic range for operation with usual input powers of a few µW.

The last detection setup is a spectrometer. It contains two rotatable gratings as dispersive elements, one with 300 and one with 1500 grooves per millimeter (Acton Spectra Pro 2750) and a liquid-nitrogen-cooled charge-coupled device (CCD) camera (Roper Scientific 7375-0001). In principle the spectrometer together with the broadband light source provides an easy tool to measure a spectrum over a large wavelength range in a short time. In practice this is limited by two factors. First, by the resolution (120 µeV and 40 µeV), which is larger than the linewidths observed in this sample. Second, by the power of the broadband light source which is distributed over a large wavelength range, therefore measuring narrow modes with low transmission requires long integration times to achieve a sufficient signal-to-noise ratio.

3.3 Spectroscopic characterization

The physics of polaritons is governed by the interplay of their light and matter constituents and their relative contribution described by the Hopfield coefficients. Due to the p–i–n structure described in Section 3.1.1 and the fiber mirror mounted on a positioner these contributions are freely tunable as we can change the relative energies between the cavity photon, the direct and the indirect exciton. To measure nonclassical correlations, the polariton interactions have to be on a comparable energy scale as the polariton linewidth. In the following sections we will spectroscopically characterize the polaritons and their components to be able to map the Hopfield coefficients to a given gate voltage and cavity length and to understand the dependences of the linewidth.

3.3.1 Exciton

To measure the properties of the excitons themselves and to understand their behaviour as function of the applied gate voltage, we mount the sample in the setup as shown in Fig. 3.3, but facing towards the window of the insert to access the sample without the cavity. This allows us to measure the spectrum as a function of the applied gate voltage by exciting the excitons with the broadband light source and detecting the reflected light with the spectrometer. In this measurement the absorption of the excitons leads to a dip in the reflection spectrum.

As a first check to see that the p–i–n structure is working as intended, we can record the I–V characteristics as shown in Fig. 3.7 **a**. The behaviour is close to what we expect from a semiconductor at cryogenic temperatures. For negative and small voltages, there are no charges that can flow through the sample and only when we start to push the Fermi level into the conduction band, mobile electrons become available. The deviation from the ideal diode behaviour between 1 V and 2 V is attributed to defects in the sample, leading to parasitic conductance channels and to a finite resistance within the doped layers. As the I–V characteristics is a bulk measurement, this finite current might not necessarily flow through the spot we measure optically where it could affect the polariton properties.

We can extract most of the information about the excitons from the reflec-

tion spectrum in dependence of the gate voltage shown in Fig. 3.7 **b**, where the dip corresponding to the excitons resonance. The two dominant features are the two ground state excitons from the thick and thin QWs which shift quadratically with gate voltage due to the dc Stark effect. Around 1.4 V and 1.8 V they hybridise with the corresponding indirect excitons, which by themselves do not couple to the photons and are only visible when they inherit oscillator strength from the direct exciton. Since in this configuration only the electrons tunnel between the QWs, the indirect excitons have an opposite dipole moment which can be seen from the corresponding slopes. Above 2 V we see a blurring of the lower exciton line, which we attribute to the presence of charges also seen in the I–V characteristic in Fig. 3.7 **a**. Figure 3.7 **b** also shows a number of higher-lying excitonic states which feature additional anticrossings. Since they are far detuned from the region of interest for this project they are not further studied.

For the remainder of this work we will only focus on the lowest-lying excitonic state, shown in the close-up in Fig. 3.7 **c** zooming into the anticrossing originating from the tunnel coupling between the two QWs. The sharp feature persisting into the anticrossing is probably a remnant from the higher-lying exciton hybridizing with the indirect exciton. Theoretical calculations on the exciton spectrum of coupled QWs done in [87] show similar features in their predictions for asymmetric QWs. Since this measurement is probing an area of several μm^2, and the QWs are not perfectly uniform in thickness, we probe excitons with an inhomogeneous distribution of energies. The resulting line shape is therefore following a Gaussian distribution from which we can extract the energy, area and width of the exciton resonances. Using a coupled oscillator model we can then fit the extracted energies and get the tunnel coupling constant $J = 2.4\,\mathrm{meV}$. In Fig. 3.7 **d** we show the area, which is a measure for the oscillator strength, and the linewidth (full width at halve maximum) of the lowest energy resonance. At 2 V the exciton is purely direct with a linewidth of 636 µeV. Reducing the gate voltage increases the indirect exciton content, leading to a drop in linewidth to a minimal value of about 424 µeV. At the same time the oscillator strength drops as well, which can be seen in the vanishing area at lower gate voltages. Above 2 V we see an additional broadening and drop in area as a result of the increased current flowing through the device. Based on this we can judge the parameter range accessible in the experiment to be between 2 V, where the

exciton is predominantly direct, and about 1.4 V, which limits the indirect exciton content to about $|c_{\mathrm{ix}}|^2 \approx 0.7$.

3.3.2 Cavity

Our open, hemispherical cavity design allows us to tune the mode energy in situ while still achieving small mode volumes. On the downside the system is more susceptible to vibrations compared to a cavity grown in one substrate (also known as monolithic microcavity). In this section we will describe how the actual cavity is formed in the experiment and look at its fundamental properties such as the linewidth, polarisation and mechanical stability. To measure the properties of the cavity and later the polaritons, the sample is mounted upside down as shown in Fig. 3.3 with the fiber approaching from the bottom. The measurements are then performed by injecting light through the fiber and detecting the transmission at the free space port. While cooling down and warming up the system, the fiber is retracted from the sample to protect both itself and the sample from getting damaged. Therefore, after each cool down the two mirrors have to be brought in proximity to each other to form the cavity. In practice we bring both parts into direct contact as this stabilizes the cavity and reduces the vibrations. The approach is done in two stages, a fast one using the stepping feature of the positioners, until the mirrors are close to touching, followed by a slow and more controlled one using the DC setting of the positioners, until the desired cavity length is reached. To know when the mirrors are almost in contact, we use the read-out of the positioners and approach the sample at room temperature while observing the fiber with a microscope. With this we can prevent damage to sample and fiber when closing the cavity. For the slow approach we send the CW laser at around 850 nm, far detuned from the exciton resonance, into the fiber and observe the transmission on the camera. When we slowly bring the fiber closer, the different longitudinal and transversal cavity modes shown in Fig. 3.9 can be observed on the camera. As the fiber and the sample surface are not perfectly parallel, there are usually three differed behaviours visible, which can also be seen in Fig. 3.8 where the transmission spectrum is recorded while the fiber is retracted from the sample. First, visible on the right side of the figure, the fiber and sample are not in contact and the different modes appear in short succession when moving the fiber. In a second

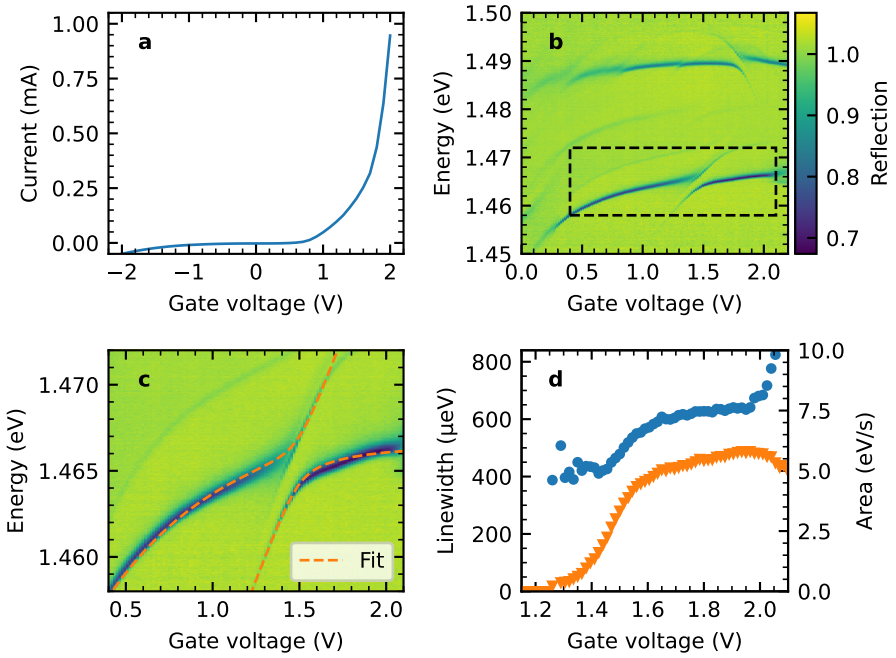

Figure 3.7: Characterisation of the QW excitons at 4 K as function of the gate voltage. **a** I–V characteristics of the sample. It closely resembles the behaviour of an ideal diode, however, defects in the sample allow for a current flow already at lower voltages than expected. **b** Extended exciton reflection spectrum. The excitons from the two QWs shift quadratically with voltage due to the Stark effect. Each of them hybridizes with an indirect exciton which depends linearly on the voltage due to their dipolar nature. **c** Close-up of the lower anticrossing, together with a fit to the coupled oscillator model. **d** Linewidth (full width at halve maximum) and area of the lower exciton branch. Both become smaller as the indirect exciton character increases.

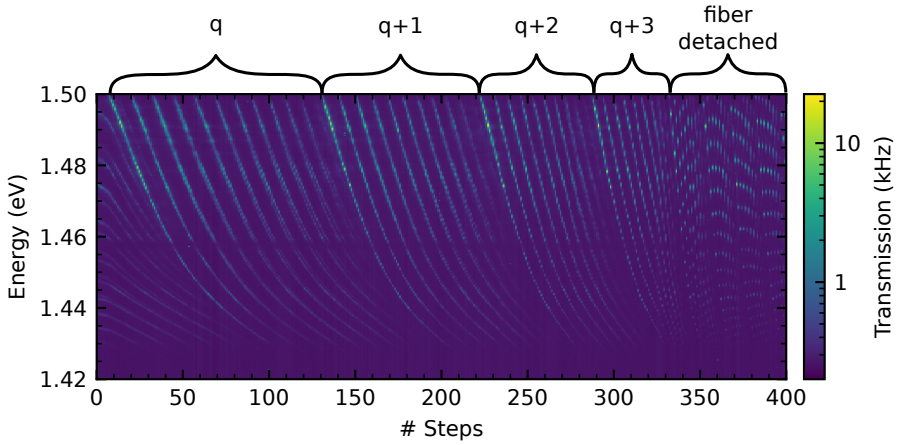

Figure 3.8: Transmission of the broadband light source recorded with the spectrometer as the cavity length is increased in small steps. For the shortest cavity length shown here, the slope of the cavity mode becomes almost flat. Here the contact between fiber and substrate is the highest. As the cavity becomes longer, the slope gradually increases as the longitudinal mode number increases by 4. At around step nr.340 the behaviour changes drastically. From here on the fiber and the sample are no longer in contact, and the modes follow in short succession when stepping further away.

stage, one edge of the fiber is touching the substrate and the rate at which modes become resonant with the laser gets slower. And finally the change in cavity length becomes very small or vanishes completely when we try to step closer. At this point we move the cavity back to the next longitudinal mode. We understand this behaviour as only the edge of the fiber touching the sample and if then the positioners try to move the fiber closer it starts to bend slightly and thus reduces the cavity length. The resulting angle change can also be seen on the camera, where the position of the cavity mode moves by several micrometres over the course of the approach. Due to this way of closing the cavity, the exact cavity length is not known, and might differ for each approach. We estimate the length to be on the order of 5 µm to 10 µm, taking into account the depth of the dimple and the penetration into the DBR mirrors.

While the tunability and the lateral confinement of the dimpled fiber mir-

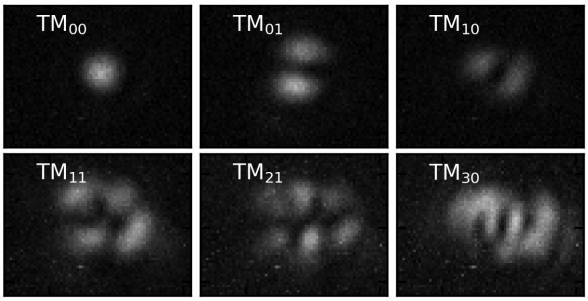

Figure 3.9: The modes of a slightly asymmetric hemispherical cavity are described by Hermit–Gauss polynomials. Using a camera and a resonant laser we can distinguish the different transverse modes and select the purely Gaussian TM_{00} to couple to the exciton.

ror are big advantages over a mirror integrated in the sample structure, it comes with a major drawback in terms of stability. Figure 3.10 **a** shows a noise spectrum measured by recording the transmission of the CW laser on the flank of the resonance, normalizing the countrate by its average and then Fourier transforming the signal. It shows a distribution of acoustic resonances situated almost entirely below 100 Hz. They originate from all possible vibrations in the surroundings, like ventilation, pumps or even from people speaking in the same room. These vibrations are transferred to the fiber and the sample and lead to fluctuations in the cavity length and therefore its energy. To shield the system from vibrations transferred through the floor or through the air, we place the cryostat on a vibration isolation stage (Thorlabs PTT600600) and put it inside a wooden box clad in sound-absorbing foam. Another measure is to decouple the pressure in the cryostat from the helium recovery system connecting all the experiments on the same floor of the building. This is done by inserting a back pressure regulator (Equilibar LF Series), which regulates the outgoing helium flow to maintain a stable pressure of around 50 mbar which is well above the pressure in the recovery line of around 10 mbar to 20 mbar. Finally, working at cavity lengths where the fiber exerts some pressure on the sample, see description above, greatly stabilizes the cavity.

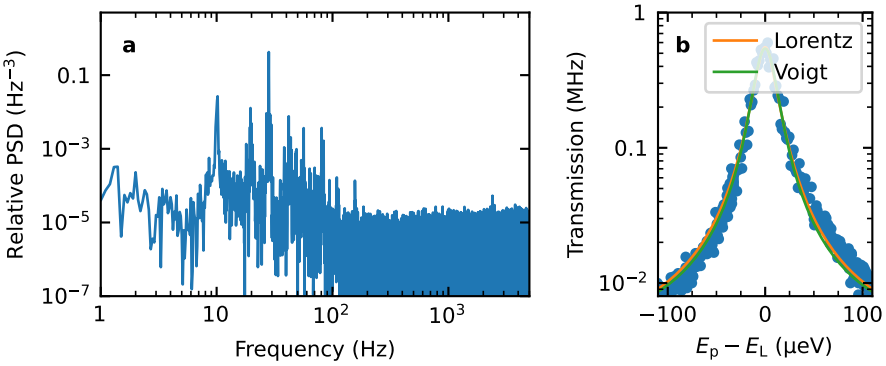

Figure 3.10: a Cavity noise spectrum obtained by Fourier transforming a normalized transmission time trace measured by exciting the cavity on the flank of the resonance. It shows that the dominant frequency components are situated below 100 Hz. **b** Fitting a Lorentzian (orange) or a Voigt profile (green) to the cavity transmission shows that both functions match equally well. If we assume the vibrations to follow a Gaussian distribution, their standard deviation is therefore smaller then the Lorentzian linewidth.

Using these precautions, the vibrations do not alter the line shape of the cavity significantly and it is still well described by a Lorentzian. As shown in Fig. 3.10 **b**, fitting the transmission with a Lorentzian and Voigt profile matches the data equally well, meaning that if we assume the underlying noise to have a Gaussian distribution, its standard deviation is significantly smaller than the Lorentzian linewidth, which is therefore sufficient to describe the mode profile. The linewidth of the bare cavity varies between 25 µeV and 30 µeV and depends on the position on the sample which could originate in the exact arrangement of the fiber with respect to the substrate or local variations in the sample quality. The amplitude of the Lorentzian corresponds to the overall transmission through the cavity, which together with the linewidth allows us to calculate the photon density inside the cavity mode. For this we also need to know the efficiency of the fiber coupling which varies for each cool down and has to be measured repeatedly. To do this we use about 1 mW input power to be able to detect the light exiting the insert from the free space port with a power meter and the measured fiber coupling efficiency is usually around 10 %. At the same time we can also

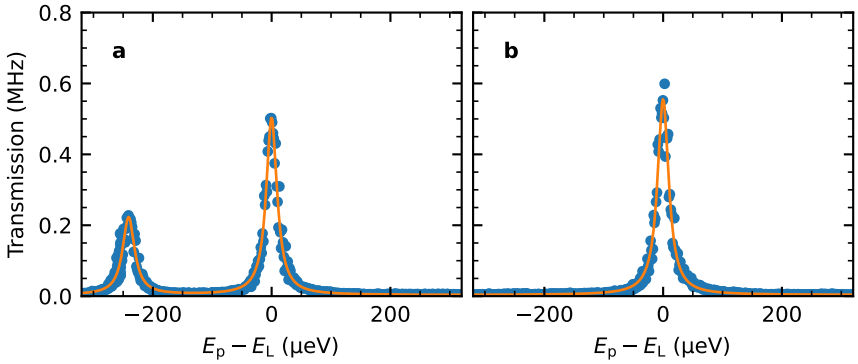

Figure 3.11: a The polarisation eigenstates of the cavity are split by about 250 µeV, while the cavity linewidth is 25 µeV in this measurement. Adjusting the input polarisation to match one mode completely suppresses the other one as shown **b**.

extract the transmission through the cavity, which is only on the order of $2 \cdot 10^{-5}$. The majority of these losses stem from the transmission inside the cavity fiber (e.g. splicing losses, damage due to bending) and measuring the transmission of a laser outside of the stop band from the input to the fiber mirror shows only about 8 % transmission. An additional source of losses is the geometric mode missmatch between the guided and the cavity mode (about 50 %) as well as the asymmetry of the mirrors (2 %). Other likely candidates explaining the losses are harder to quantify, and we expect the angle between the cavity and the fiber, a potential offset of the fiber core to the dimple and absorption in the DBRs, the doping layers or the GaAs growth substrate to play a role.

While in principle the solution for the hemispherical optical cavity would result in circularly polarized Laguerre–Gauss modes, a birefringence in the GaAs substrate breaks the translational symmetry, resulting in linearly polarized Hermite–Gauss modes. By measuring the transmission of circularly polarized light we can measure the resulting polarisation splitting (see Fig. 3.11 **a**) of 250 µeV, which is significantly larger than the linewidth. While the splitting is reduced for polaritons according to their photonic fraction, for the parameter range in our experiments the splitting will remain larger than the linewidth and we can treat them as two separate states. By adjusting

the input polarisation using the polarisation optics described in Section 3.2.2, we can select one of the modes while completely suppressing the other, as is shown in Fig. 3.11 **b**.

3.3.3 Polariton

By tuning the cavity energy close to the exciton resonance the system enters the strong coupling regime and forms polaritons. In Fig. 3.12 we show the transmission spectrum for three different gate voltages as we sweep the dc voltage of the positioners to change the cavity length. In addition to the prominent longitudinal mode, we observe various transversal modes which also couple to the exciton. As they belong to sets of modes with different longitudinal mode numbers, they have different slopes, and since the excitation and collection uses single mode fibers, their overlap is reduced and they are much fainter in the spectrum. As we showed in Fig. 3.7, the exciton is entirely direct at 2 V and there is no contribution of the indirect exciton, so we only see one anticrossing at the energy of the direct exciton. As we lower the gate voltage, the excitons hybridize and form two new eigenstates, both with a sizable oscillator strength, which shows up as two anticrossings in the spectrum. As we lower the energy of the indirect exciton further, the lower-energy hybridized exciton loses oscillator strength and the corresponding anticrossing gets smaller and shifts to lower energies. Fitting the peak energies to the corresponding coupled oscillator model (result shown as red dashed lines), we can extract the cavity-exciton coupling constant $\Omega = 1.001(3)\,\mathrm{meV}$ and the tunneling constant $J = 1.355(9)\,\mathrm{meV}$. Using these parameters we can extract the Hopfield coefficients for the polariton branches shown for the lower polariton in Fig. 3.13. It shows how we can tune the polariton composition by changing the cavity length and the gate voltage.

In Fig. 3.14 **a** the linewidth and the area of the lower polariton resonance without indirect exciton contribution is shown as function of the cavity length. The linewidth initially decreases from the value of the bare cavity down to about 15 µeV. This is a consequence of the exciton linewidth being dominated by inhomogeneous broadening as shown in Fig. 3.7, while the non-radiative decay of the exciton is orders of magnitudes smaller. Due to the strong coupling, the polariton is far detuned from the tails of the

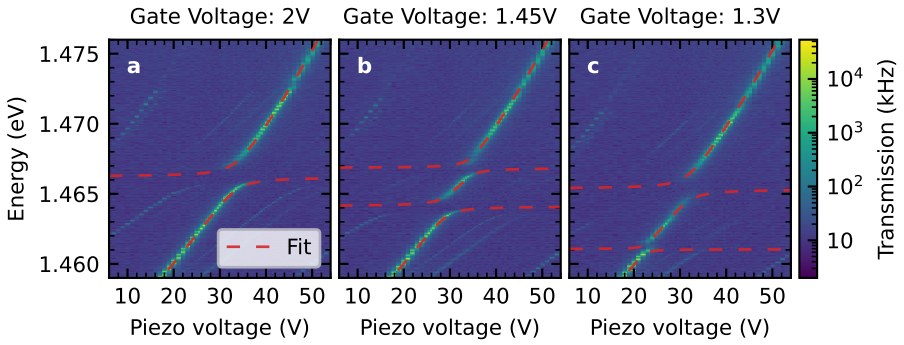

Figure 3.12: Polariton transmission spectrum as function of cavity length for different gate voltages. It shows the energy of the cavity mode scaling almost linearly with its length and the hybridisation with the excitonic states. Going from left to right the indirect exciton is tuned past the direct exciton mode from being tuned to higher energies at 2 V, to being on resonance at 1.45 V to finally being slightly below the resonance at 1.3 V. The red dashed lines correspond to a fit to the model described in Eq. (2.15) and show good agreement with the transmission data.

inhomogeneous distribution, and only the non-radiative decay of the exciton contributes to the polariton linewidth [76]. We model the behaviour of the linewidth, see blue line in Fig. 3.14 **a**, using $\gamma_{\text{inhom}} = 320\,\mu\text{eV}$ and $\gamma_{\text{non-rad}} = 5\,\mu\text{eV}$ and get a good agreement with the data. As we tune the polariton closer to the exciton it starts to overlap with the tails of the inhomogeneous distribution and as a consequence the linewidth drastically increases. This is at the same time accompanied by a very abrupt decrease of the area and thus the oscillator strength of the lower polariton. This protection from the inhomogeneous exciton broadening allows us to measure narrow polariton linewidths, but it also introduces a limit on how much indirect nature we can impose before the line broadening and loss of oscillator strength becomes sizable.

3.4 Correlation measurement

To understand interaction-induced quantum correlations in exciton–polaritons, we measure the second-order correlation function introduced

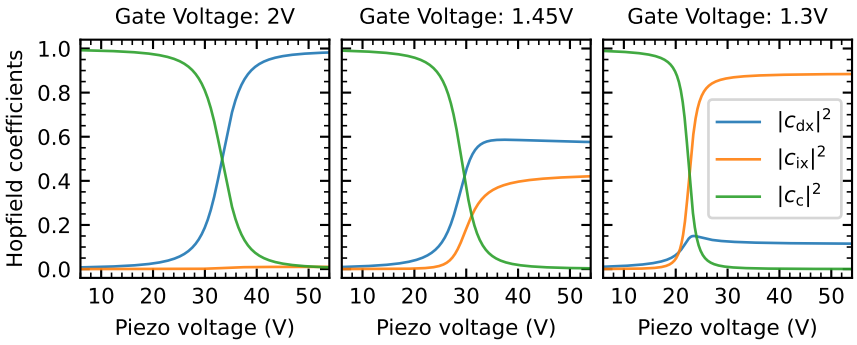

Figure 3.13: Hopfield coefficients as a function of the cavity length extracted from the fits shown in Fig. 3.12. At a gate voltage of 2 V (**a**) the indirect exciton content $|c_{ix}|^2$ is zero and changing the cavity length tunes the lower polariton between being cavity like to being exciton like. At lower gate voltages (**b** and **c**) the direct- and indirect exciton are hybridised and the polariton is a mixture of all three components.

in Eq. (2.26) for different sets of parameters defining the polariton properties. To first order we expect the correlations to depend on the excitation power, the relative detuning between the laser and the polariton $\Delta/\Gamma_p = (E_p - E_L)\,\Gamma_p$, the polariton–polariton interaction strength (U_{pp}) and the linewidth (Γ_p). While we can directly control the first two parameters in the experiment, the last two are defined by the polariton composition, controlled experimentally by the gate voltage and the cavity length.

Having this free tunability of the cavity length is made possible by the open cavity design but it also makes the cavity susceptible for mechanical instabilities. The sensitivity of the measurement to energy fluctuations is best seen in the detuning dependence of the correlations shown in Fig. 2.10 which shows that even energy shifts of a fraction of the linewidth substantially alter the magnitude of the correlations. Overcoming these instabilities is one of the main experimental challenges in this work. They extend over a wide range of timescales, as illustrated in Fig. 3.15 on the left, and are governed on one end by slow drifts, such as creeping of the piezos, and on the other end by acoustic vibrations as shown in the noise spectrum in Fig. 3.10, that lead to fluctuations of the cavity length on timescales on the order of

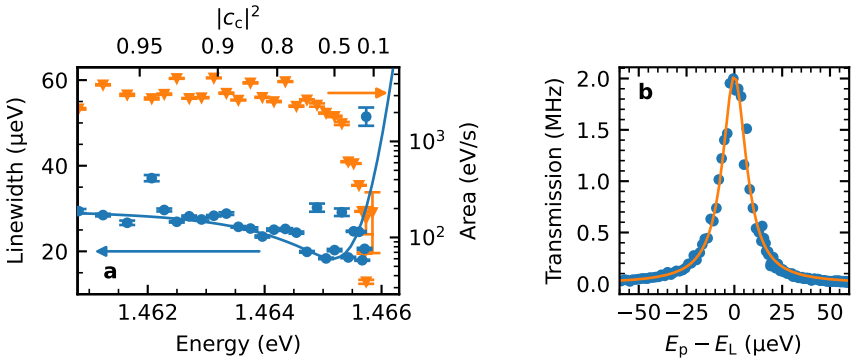

Figure 3.14: a Linewidth and area of the direct exciton–polariton (2 V) as function of its energy (bottom axis) and the corresponding cavity content (top axis). As the strong coupling protects the polariton from the inhomogeneously broadened exciton distribution, the linewidth initially decreases. Only when the polariton energy gets close to the tails of the inhomogeneous exciton distribution, its linewidth increases abruptly accompanied by a drop in oscillator strength, indicated by the area (orange triangles). The theoretical model discussed in Section 2.3.3 (blue line) with $\gamma_{\text{inhom}} = 320\,\mu\text{eV}$ and $\gamma_{\text{non-rad}} = 5\,\mu\text{eV}$ shows good agreement with the data. **b** Transmission spectrum of a polariton mode with the corresponding Lorentzian fit. The linewidth is about 15 μeV, corresponding to the minimum shown in **a**.

tens of milliseconds. Simultaneously the integration time of the experiment is dictated by the signal-to-noise of the coincidences. The number of coincidences is thereby given by $C = \tilde{n}^2_{\text{photon}} t_{\text{int}} \Delta\tau$, where $\tilde{n}_{\text{photon}}$ is the incoming photon rate which in this experiment is on the order of a few megahertz, $\Delta\tau$ is the bin size of the coincidence histogram which has to be shorter than the polariton lifetime and therefore is on the order of tens of picoseconds, and t_{int} is the integration time. For a standard experimental setting the resulting coincidence rate is on the order of one to ten coincidences per second and due to the fluctuations not all coincidences can be accounted for in a given histogram. Therefore the required integration times to overcome the shot noise span from a few hours up to a day, depending on the overall transmission and the size of the correlation feature.

To deal with these experimental challenges we combine different methods into our measurement procedure, which is illustrated in Fig. 3.15. The figure

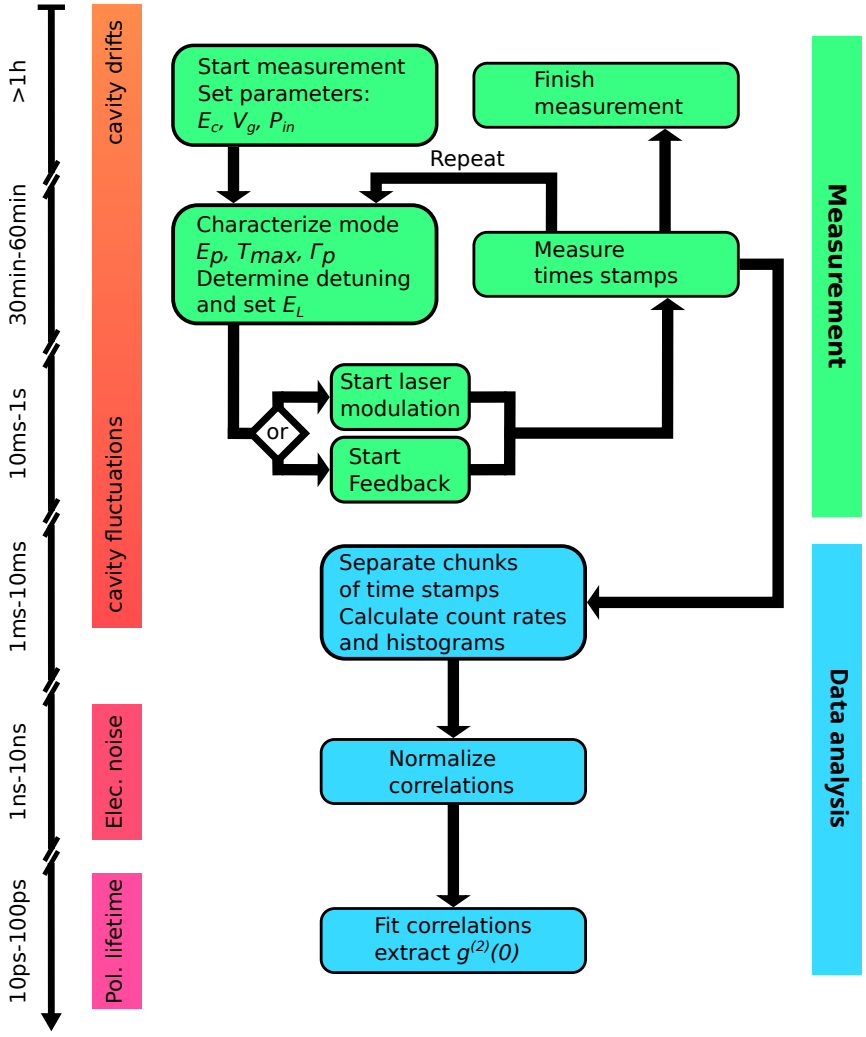

Figure 3.15: Diagram illustrating the measurement and data analysis process. On the left we indicate the relevant timescales on which each element operates, together with the relevant physical processes.

shows the order of the different processes within the measurement sequence (black arrows) and on which timescales these processes act, together with the relevant physical processes indicated on the left. The whole measurement with a given set of cavity length, gate voltage and input power is therefore defining the longest timescale and it can take several hours to acquire enough signal to overcome the noise. To account for slow drifts which, after long integration times could potentially affect the polariton energy and linewidth, we perform shorter sub-measurements, which are repeated multiple times. In each repetition we first characterize the line shape of the mode to calculate the relative detuning Δ/Γ_p of the laser and at the end of the iteration we sweep the gate voltage between $-2\,\mathrm{V}$ to $2\,\mathrm{V}$ to flush out charges which might accumulate after prolonged exposure of the sample. Within each repetition we implemented two separate methods which account for faster drifts and/or slower fluctuations of the cavity length. The first one is a slow modulation of the laser which we describe in more detail in Section 3.4.3 and allows us to track the changes in the detuning between the cavity and laser energy. The second alternative is an active feedback on the piezo controlling the cavity length, which we describe in Section 3.4.2. A final method which we us in combination with either of the previous ones, is postselection of the data. For this purpose we cut the sequence of time stamps obtained from the TCSPC electronics into shorter chunks and by calculating the countrate for each chunk we can sort the corresponding histogram according to the countrate. This allows us to resolve correlations at a speed limited only by the countrate of the transmitted photons, which ultimately defines the rate of information we can get from the system.

In principle it would be possible to beat this limit by using a separate cavity mode to gain information about the cavity length. If this mode is sufficiently far detuned, it will not couple to the excitons and can therefore be driven at a higher power. We tested this approach by using the next lower-energy longitudinal cavity mode, located about 70 meV below the exciton, to track fluctuations of the cavity length. Since the transmission through the cavity is lower at the edge of the stop band, higher powers are necessary to substantially increase the countrate. It turned out that pumping the second cavity mode with powers of only $100\,\mu\mathrm{W}$ already results in broadening of the polariton, which makes it unfeasible for our purposes.

3.4.1 Postselection

By directly recording the time stamps of photon arrival events we not only gain access to the histogram of coincidences, we can also track the photon countrate transmitted through the cavity. Therefore we can cut the stream of arrival times into individual chunks and calculate the coincidence histogram and the average countrate for each chunk. This is then used to assign the corresponding histogram to a relative detuning, illustrated in Fig. 3.16, which can be calculated using the parameters from the Lorentzian line shape $|\Delta|/\Gamma_\mathrm{p} = 0.5\sqrt{A/\tilde{n}_\mathrm{photon} - 1}$, where A is the amplitude of the Lorentzian. It is crucial to note that we cannot distinguish between positive and negative detunings using this formula and we need to combine this postselection process with the laser modulation or the active feedback that we will describe in the next sections. Over the duration of a measurement we record a distribution of countrates as shown in the example in Fig. 3.16 **b**, and after assigning them to a detuning we can sum together the corresponding $g^{(2)}$ histograms. In practice we cannot load chunks of timestamps after equal integration

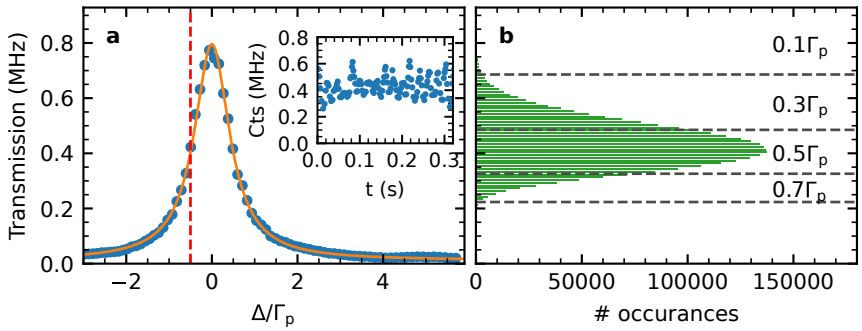

Figure 3.16: a Lorentzian line shape of the polariton and time trace of the countrate of each measurement chunks when exciting with a laser at $\Delta = -0.5\,\Gamma\mathrm{p}$ (red line). **b** Histogram describing the number of measurement chunks occurring at a given countrate. Using the parameters obtained from the fit (orange curve) we can assign each of these chunks to a relative detuning $|\Delta|/\Gamma_\mathrm{p}$, shown by horizontal lines for 0.1, 0.3, 0.5 and 0.7.

times, so we fix the chunk size to $2^{11} = 2048$ timestamps. This is a compromise of beating the shot noise when calculating the countrate ($\sqrt{2048} = 45$)

and achieving a timing resolution below the vibrational timescales. A quick estimate shows that with countrates between a few hundred kHz and a few MHz we will achieve a timing resolution of one to ten milliseconds, which is slightly shorter then the 10 ms expected from the vibration spectrum shown in Fig. 3.10 **a**.

3.4.2 Stabilisation

A first method that we use in combination with the postselection scheme to counteract drifts and slow fluctuations of the cavity length is an active feedback controlling the cavity length, illustrated in Fig. 3.17. By using the signal from the detector as an input for a PID controller, we can generate a response proportional to the displacement of the cavity and send it to the positioner to correct for the displacement. As the PID requires an dc signal for the regulation, the pulses from the detectors are first amplified and then converted to an dc signal via a counter, which counts the number of pulses in a given integration time and then creates a proportional dc voltage.[1]

The response times of these devices are very fast and the speed of the regulation is most likely limited by the positioners moving the fiber. The corresponding timescale is hard to assess and depends on the positioners and on the particular way of contact between the fiber and the substrate. By an abrupt change of the cavity length and the resulting recovery of the countrate we can estimate the response time of the PID system, which is on the order of tens of milliseconds. While this is too slow to completely counteract the vibrations in the system, it can suppress some of the slower components and compensate for absolute drifts of the cavity length. Therefore by choosing a large enough detuning between the excitation laser and the polariton (around $\Delta/\Gamma_p = 0.5$), the stabilisation ensures that the sign of the detuning remains constant over a measurement and in combination with the postselection scheme described above, allows us to measure correlations

[1] In a first iteration we used a National Instruments USB-7855R field-programmable gate array (FPGA), which is directly programmable using LabView, to simultaneously implement the counter and the PID. Due to technical problems we had to switch in a second iteration to a redpitaya STEMlab125-14 FPGA programmed by Yu Liu in a research project at the "Quantum Optics" group led by Prof. Tilman Esslinger at ETH and a Stanford Research Systems SIM960 PID.

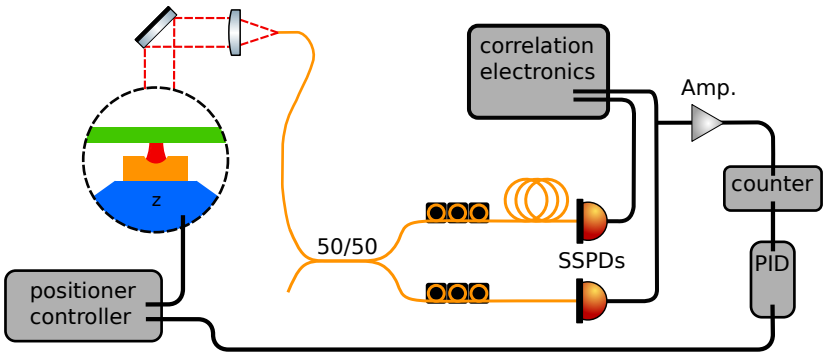

Figure 3.17: Schematic of the stabilisation setup. The photons transmitted through the cavity are detected on the SSPDs which create a voltage pulse for every photon. These pulses are split off, amplified and then converted to a dc signal which serves as an input for a PID controller. The response is then added to the voltage of the positioners to counteract the displacement of the cavity.

at a well-defined laser detuning. One limitation of this method is that the PID needs a finite slope of the resonance to create a feedback and therefore measurements on resonance are not possible.

3.4.3 Laser modulation

Our second method used in combination with the postselection scheme is a slow modulation of the laser wavelength over the polariton resonance. By analysing the transmission over time we can determine the sign of each data chunk. Fig. 3.18 shows the Lorentzian line shape of the polariton and the modulated transmission of the first 2 min of a measurement as a result of the laser modulation shown below. The initial points (gray), where the laser wavelength is tuned to the starting point, are discarded and starting from the first maximum we can distinguish between positive (blue) and negative (red) detuning and assign Δ/Γ_p as described in Section 3.4.1 to each data chunk. In practice, the wavelength modulation is done in a range of $-0.5\,\Gamma\mathrm{p}$ to $0.5\,\Gamma\mathrm{p}$ and back in 40 discrete steps each lasting 1 s.

This way of measuring correlations allows us to directly probe the different detunings in one measurement, including on the resonance. This is not pos-

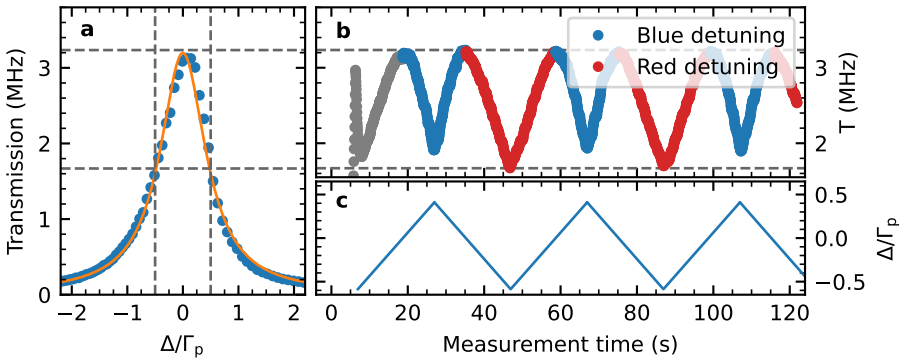

Figure 3.18: a Polariton mode together with the average countrate for each measurement chunk **b** modulated by sweeping the laser between $-0.5\,\Gamma$p to $0.5\,\Gamma$p (**c**). By counting the maxima of the transmission we can assign each measurement chunk to positive or negative laser detunings Δ.

sible using the active stabilisation, as the PID requires a slope to calculate a proportional feedback.

3.4.4 Data analysis

To obtain $g^{(2)}(\tau)$ from the transmitted photons, we measure the waiting time distribution between photon arrival times using two SSPDs in a HBT-type configuration and TCSPC electronics. Since the detectors have to recover the superconducting state after each photon absorption event, they are blind to successive photons for a short period of time on the order of tens of nanoseconds. As we expect the polariton correlations to occur within this dead time, we can restrict ourselves to measure cross-correlations between the photon arrivals at the two detectors.

As in principle the statistical properties of the transmitted photons can be altered by external fluctuations on all timescales, for example the oscillations from the electronics discussed in Section 3.2.2. The proper normalisation of the coincidences is difficult and potentially one would have to measure on very long timescales to obtain the true steady state value for normalisation. But since we are only interested in short timescales on the order of the polariton lifetime, we can treat the data beyond 1 ns as background. Fig. 3.19 **a**

shows the raw histogram with a clear bunching background on timescales of 19 ns. The gray area shows a window of 1 ns which is removed to fit the background using an exponentially decaying function (orange line). With the result from the background fit we can then normalize the coincidences and fit them as shown in Fig. 3.19 **b**. To extract the value of $g^{(2)}(0)$ from the data we use a heuristic model represented by a two-sided exponential decay convoluted with a Gaussian function describing the jitter from the detection setup described in Section 3.2.2 ($\sigma_{\mathrm{sys}} = 13.9\,\mathrm{ps}$),

$$g^{(2)}(\tau) = \left(1 - \left(1 - g^{(2)}(0)\right) e^{-\frac{|\tau-\tau_0|}{\delta}}\right) * \mathcal{G}\left(\sigma = \sigma_{\mathrm{sys}}\right), \tag{3.1}$$

where τ_0 is the zero time delay of the detection setup, δ is the associated time scale proportional to the polariton lifetime and $\mathcal{G}$ is the normalized Gaussian distribution. Even though this model is not derived from Eq. (2.26) and the polariton Hamiltonian, it allows us to extract the value of $g^{(2)}(0)$ and its uncertainty considering the noise in the data and the jitter of the detection setup. If there is no bunching or antibunching feature in the correlations, the fit tends to minimize the residuals by matching a small antibunching or bunching peak to points in the noise. Since these values have no physical meaning, we set $g^{(2)}(0) = 1$ with an uncertainty corresponding to the standard deviation of $g^{(2)}(\tau)$.

The dip shown in Fig. 3.19 was measured with a polariton without indirect exciton content and $|c_{\mathrm{c}}|^2 = 0.45$ while exciting at a relative laser detuning $\Delta/\Gamma_{\mathrm{p}} = -0.5$ using the stabilisation and postselection scheme described above.

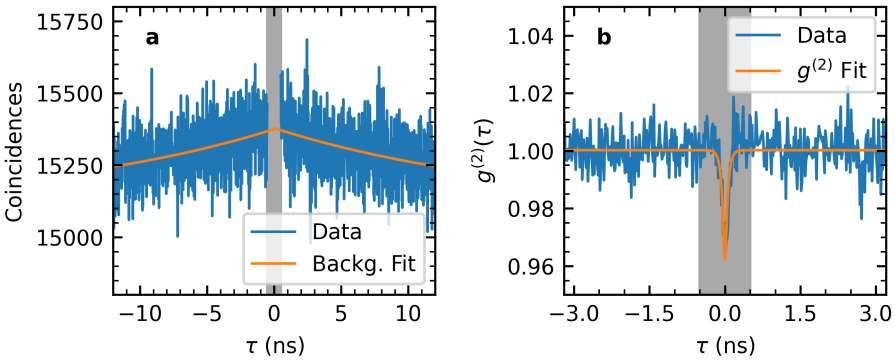

Figure 3.19: **a** Unnormalized second-order correlation function. The short timescales (gray area) are removed from the histogram of photon arrival time differences to fit an exponential decay (orange line) to the data. This is then used to obtain the normalized $g^{(2)}$ shown in **b**. By fitting Eq. (3.1) to the data we obtain the depth and with of the dip, in this example: $g^{(2)}(0) = 0.953(5)$ and $\delta = 51(8)$ ps.

CHAPTER 4

Polariton correlations

The observation of sub-Poissonian statistics is a benchmark for quantum correlations in a system. By measuring the second-order correlation function of exciton–polaritons we observe clear signatures of non-classical physics. For direct exciton–polaritons with a high exciton content we observe a clear 10 % antibunching dip originating from the interaction-induced anharmonicity of the polariton manifold, while measurements at lower exciton contents show a small, detuning–independent antibunching which cannot be explained by interactions. We attribute this to a "dissipative blockade" mechanism, induced by the selective coupling to the biexciton. We observe no enhancement of the interaction strength for indirect excitons, due to the simultaneous reduction of the oscillator strength resulting n a broadened linewidth and reduced transmission.

4.1 Direct exciton–polaritons

4.1.1 Power dependence

From theoretical calculations [25] we expect the correlations of the polaritons to become weaker as we cross a certain density threshold with increasing excitation power. At the same time we are interested in measuring at high countrates to reduce the overall measurement time. In this section we will

explore the dependence of $g^{(2)}$ on the input power to find optimal conditions for extended correlation measurements.

To measure the power dependence we excite polaritons with $|c_c|^2 = 0.45$ and no indirect exciton content with a detuning from the excitation laser of $\Delta/\Gamma_p = -0.5$ and measure correlations using the stabilisation and postselection scheme described in Section 3.4. The power values refer to the power measured at the fiber connection of the cryogenic insert Fig. 3.3. The number of photons actually coupling into the cavity are orders of magnitudes smaller due to losses in the fiber (splicing, bending, etc.) and the mismatch between the guided and the cavity mode. We stabilize the power using a PID controller as described in Section 3.2.2 and measure in the range of 0.2 µW to 10 µW.

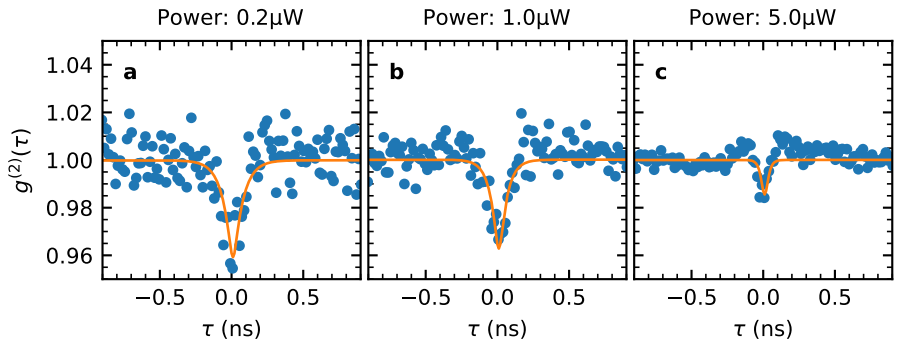

Figure 4.1: Measured $g^{(2)}$ at three increasing input powers for a polariton with no indirect exciton content and $|c_c|^2 = 0.45$ excited at a relative laser detuning $\Delta/\Gamma_p = -0.5$. The antibunching dip becomes smaller and narrower with increased power and **c** shows the onset of oscillations as small bunching features. The results of the fits (orange curves) for these and additional power levels are shown in Fig. 4.2.

In Fig. 4.1 we show the measured $g^{(2)}$ data together with the best fit for three different powers. It shows the reduction in magnitude and timescale of the antibunching, and for the highest powers we can distinguish additional bunching on either side of the dip. We attribute this bunching to the onset of oscillations proportional to timescales given by the laser detuning Δ (we will come back to this observation in the next section when discussing the detuning dependence of $g^{(2)}$). As for lower powers this feature remains below

the noise. The fit results for all powers, together with the corresponding linewidth and polariton density obtained from transmission measurements are shown in Fig. 4.2. We calculate the density from the photon countrate using $\tilde{n}_{\mathrm{det}} = n_{\mathrm{p}}|c_{\mathrm{c}}|^2\eta\kappa/\tau_{\mathrm{p}}$, where $\tilde{n}_{\mathrm{det}}$ is the detected countrate, η an estimate of the collection and detection efficiency[1], τ_{p} the cavity lifetime assuming that the transmission through the mirrors is the dominant loss mechanism and $\kappa = 0.98$ describes the imbalance of the mirrors. The transmission data in Figs. 4.2 **a** and 4.2 **b** shows the expected increase of the polariton density with power, which is accompanied by a significant line broadening. At the same time the correlation fit results in Figs. 4.2 **c** and 4.2 **d** show the reduction in magnitude and timescale of the antibunching dip.

While power broadening could be a potential explanation for these observations, at these low densities the effect is negligible. It is more likely that the power dependent line broadening and loss of correlations originate from dephasing processes [60, 88] or from heating of the DBRs or the GaAs substrate. We should also keep in mind that the overall transmission is only on the order of 10^{-5}, and a significant number of photons could reach the DBRs or the substrate without contributing to the polariton population. To asses which effect plays a role, we model the influence of dephasing and heating in our system using a numerical model (see Appendix A) and compare it to the measurement.

We can describe the loss of coherence due to dephasing by adding an additional collapse operator $\sqrt{0.5\,\Gamma_{\mathrm{deph}}}\,p^\dagger p$ to the model. Further we assume the dephasing to be negligible at the lowest power and set $\Gamma_{\mathrm{p}} = \Gamma_{\mathrm{meas}}(200\,\mathrm{nW}) = 14.2\,\mu\mathrm{eV}$, such that the measured, power-dependent linewidth is given by $\Gamma_{\mathrm{meas}}(P) = \Gamma_{\mathrm{p}} + \Gamma_{\mathrm{deph}}(P)$. By fixing the detuning $\Delta = -0.5\,\Gamma_{\mathrm{meas}}$ we can simultaneously fit n_{p} and $g^{(2)}(0)$, where the only free parameters are the polariton interaction strength and a proportionality factor between the input power and the effective polariton driving strength. The best fit is shown in Figs. 4.2 **a** and 4.2 **c** (orange line), for better visibility we interpolate the linewidth to plot a solid curve. It shows that the effect of dephasing on correlations is much stronger then what we observe in our data.

[1] η includes the fiber coupling efficiency measured at each cool down, the transmission through the optical fibers and the quantum efficiency of the SSPDs (Fig. 3.5).

To estimate the effect of line broadening due to absorption of photons in the DBRs or the GaAs substrate, we can use Eq. (2.27) assuming a power dependent linewidth

$$g^{(2)}(P) = 1 - U_{\mathrm{pp}}/(A\Gamma_{\mathrm{p}}(P)). \tag{4.1}$$

We can calculate the interaction strength using the lowest power $U_{\mathrm{pp}} = A\Gamma_{\mathrm{p}}(P_0)(1 - g^{(2)}(P_0))$ with $P_0 = 200\,\mathrm{nW}$ and get a good agreement with the data (Fig. 4.2 **c** dashed green line). We can also fit n_{p} and $g^{(2)}(0)$ to our numerical model fixing $\Gamma_{\mathrm{p}} = \Gamma_{\mathrm{meas}}$, which agrees well with the data (solid green line in Figs. 4.2 **a** and 4.2 **c**). From the fit we can also extract the polariton–polariton interaction strength $U_{\mathrm{pp}} = 0.61(3)\,\mu\mathrm{eV}\mu\mathrm{m}^2$ for the given Hopfield coefficients.

Based on the simulations and our estimate of the polariton number being well below one, we conclude that the reduction of antibunching with increased power originates from line broadening through photon absorption that results in heating of the mirrors or the substrate. Therefore the appropriate input power for correlation measurement can be chosen by observing the linewidth of the polaritons and remaining below the threshold of line broadening.

4.1.2 Detuning dependence

In this section we use the laser modulation and postselection procedures described in Sections 3.4.1 and 3.4.3 to measure how polariton correlations depend on the relative laser detuning $\Delta/\Gamma_{\mathrm{p}}$ for polaritons with different direct exciton contents. All measurements were done at a gate voltage of 2 V, where the indirect exciton is far detuned and at powers below the onset of line broadening described in Section 4.1.1. An overview of the data as function of the cavity content and three different laser detunings is presented in Fig. 4.3. We observe four regimes separated by vertical lines in the plot, where the correlations behave substantially different.

For cavity contents above $|c_{\mathrm{c}}|^2 = 0.65$ the exciton content is too low to contribute to sizable polariton–polariton interactions and we observe the classical coherence inherited from the laser. On the other end, for the largest measurable exciton content, we observe the "S" shape, shown in Fig. 4.4 **a**, expected from the polariton Hamiltonian in Section 2.4.2. The interactions

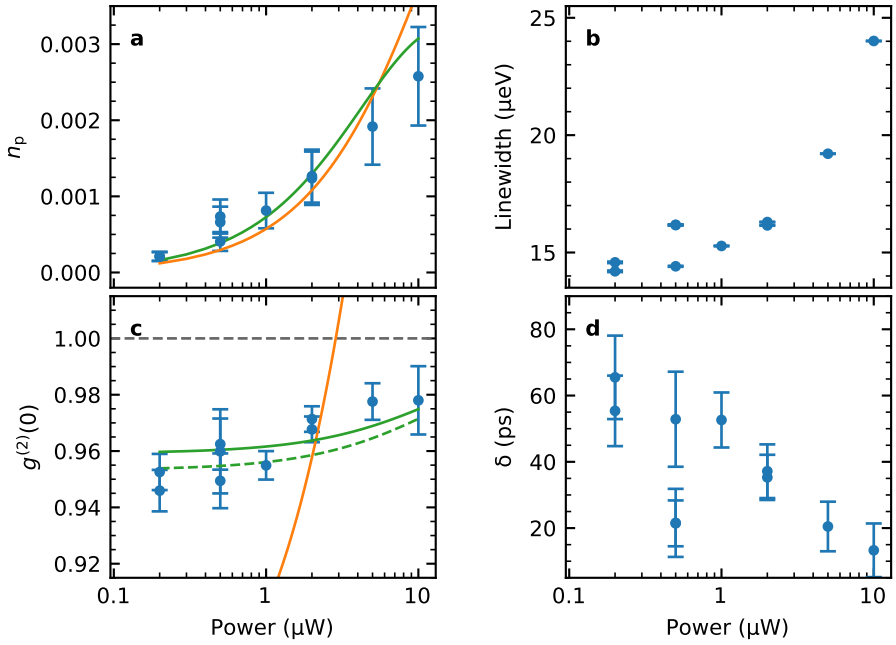

Figure 4.2: Power dependence of the polariton density (**a**), linewidth (**b**), $g^{(2)}(0)$ (**c**) and antibunching time scale (**d**). As already shown in Fig. 4.1, the dip becomes smaller and narrower with increased power. This reduction in $g^{(2)}(0)$ originates from the increase in Γ_p. A simultaneous fit of n_p and $g^{(2)}(0)$ with a model assuming line broadening due to dephasing (orange curve) or an increase of the intrinsic linewidth (green curve) shows that the latter agrees well with the data. We attribute the line broadening to heating, for example of the cavity mirrors, and a resulting decrease in cavity lifetime.

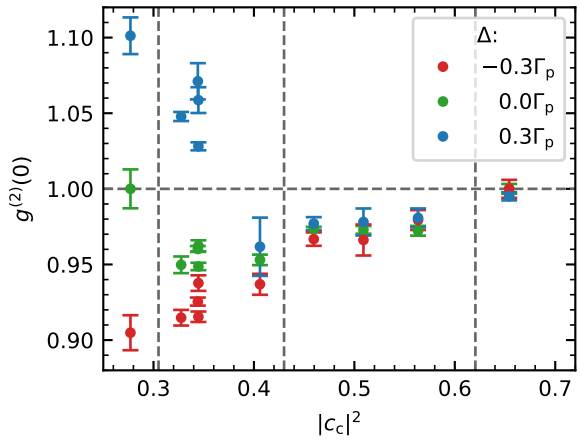

Figure 4.3: $g^{(2)}(0)$ as a function of the cavity content for three different laser detunings Δ/Γ_p. We can distinguish four regimes showing a different type of behaviour. At the highest cavity content the polariton–polariton interactions are to weak and we observe no correlations within the measurement uncertainty. Between $|c_\mathrm{c}|^2 = 0.45$ and $|c_\mathrm{c}|^2 = 0.55$ we observe a detuning-independent antibunching of about 0.97 which crosses over in an intermediate regime before showing the expected "S" shape at $|c_\mathrm{c}|^2 = 0.28$ with bunching on the blue side, coherent statistics on resonance and antibunching on the red side.

mediated by the exciton are strong enough to shift the $|2p\rangle$ polariton state, introducing an anharmonicity to the polariton manifold. Therefore when exciting the polariton on the red side, the laser energy is detuned from the transition to the $|2p\rangle$ polariton state and we observe sub-Poissonian statistics with an antibunching dip $g^{(2)}(0)$ =0.90(1) shown in Fig. 4.4 **c**. By exciting the polariton on the blue side, the laser energy is close to the resonance of the two-polariton transition and we observe super-Poissonian statistics with a bunching peak of about $g^{(2)}(0)$ =1.10(1) shown in Fig. 4.4 **e**. The two effects cancel if we excite exactly on resonance and $g^{(2)}(\tau) = 1$ as shown in Fig. 4.4 **d**. We can fit the numerical model described in Appendix A to the data and extract the polariton–polariton interaction strength $U_\mathrm{pp} = 6.0(3)\,\mu\mathrm{eV}\mu\mathrm{m}^2$. The time scales associated with the correlations are plotted in Fig. 4.4 **b**, where they show a maximum close to $\Delta/\Gamma_\mathrm{p} = 0$ and then decay on both sides. Since the correlations describe the excitation of a second polariton conditioned on

the presence of a first one, we expect the timescales to be proportional to the occupation probability of the single-polariton state. The transient solution to the equation of motion Eq. (2.19) results in $\langle n_1(t)\rangle \propto \exp\left(-(\Gamma_\mathrm{p} + i2\Delta)t\right)$ with two relevant timescales. Therefore for finite detunings, the population oscillates proportional to Δ which can then be observed as a shortening of the timescales in $g^{(2)}$. This is also the origin of the bunching feature on either side of the antibunching dip we observed in Fig. 4.1 **c**, showing the onset of oscillations in $g^{(2)}$.

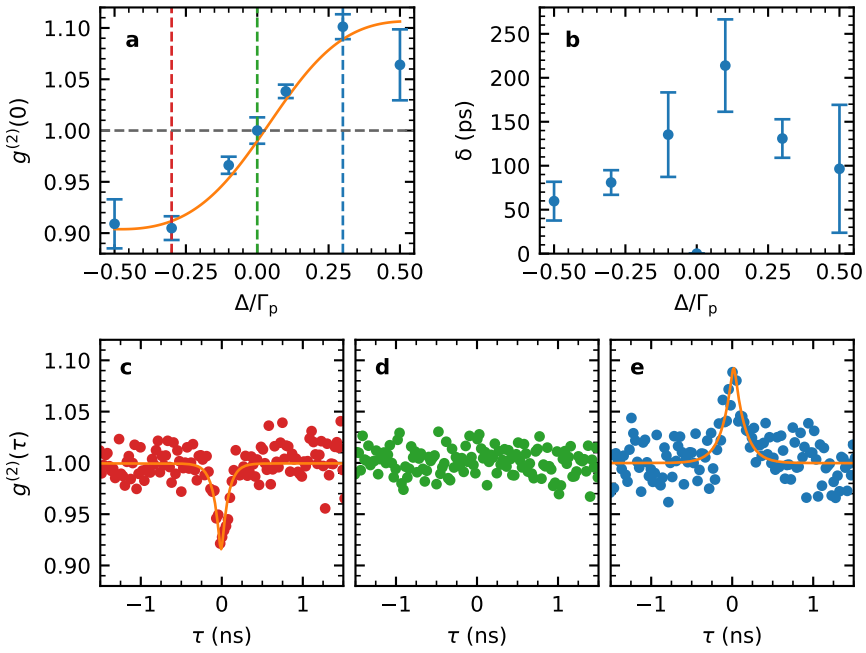

Figure 4.4: **a** Detuning dependence of $g^{(2)}(0)$ at $|c_\mathrm{c}|^2 = 0.28$, **b** the corresponding timescales δ and **c** to **e** time-dependent correlations $g^{(2)}(\tau)$ marked by vertical lines in **a**. We clearly observe a "S"-shaped curve expected for weakly interacting polaritons ($U_\mathrm{pp} < \Gamma_\mathrm{p}$) and the best fit to the numerical model yields $U_\mathrm{pp} = 6.0(3)\,\mu\mathrm{eV}\mu\mathrm{m}^2$. The correlation timescales δ decrease as function of the detuning as the coupling within the polariton manifold becomes faster. While **c** and **e** show a peak/dip with the corresponding best fit, there is no feature in **d** to fit, so the corresponding value and errorbar in **a** are the mean and standard deviation of $g^{(2)}(\tau)$.

If we reduce the cavity content to $|c_c|^2 = 0.46$ the dependence of $g^{(2)}(0)$ with Δ/Γ_p changes significantly. The data in Fig. 4.5 shows that instead of the expected "S"-shaped curve, we observe an antibunching dip independent of the laser detuning. This behaviour is also replicated by measurements at $|c_c|^2 = 0.51$ and $|c_c|^2 = 0.56$ as shown in Fig. 4.3. This detuning-independent antibunching is not captured by the basic polariton Hamiltonian (Eq. (2.15)) and suggests a sizable coupling to an additional state. Based on the extended range of this feature and the fact that we see no alteration in the polariton linewidth, we expect it to be broad and relatively weakly coupled to the polariton. We will explore the coupling to the biexciton resonance as a possible explanation in Section 4.1.3.

Between $|c_c|^2 = 0.33$ and $|c_c|^2 = 0.41$ we observe an intermediate regime, shown in Fig. 4.6. For the negative laser detuning in Fig. 4.6 **c**, we see the expected antibunching dip which gets smaller closer to resonance. The dip then stays constant and persists on top of a bunching peak observed for positive detunings, shown in Fig. 4.6 **e**. By separating the timescales we can fit both features independently, leading to the two values shown in Figs. 4.6 **a** and 4.6 **b** for positive detunings. This behaviour suggests a combination of the "S" shape we observe at $|c_c|^2 = 0.28$ and the flat antibunching around $|c_c|^2 = 0.5$. Since both contributions lead to a dip for negative detunings, we cannot distinguish them as their timescales are too similar. As we approach the resonance the contribution of the polariton interactions get smaller and only the correlations from the detuning-independent feature remain. For positive detunings they again increase, leading to bunching, while the detuning-independent feature remains as a dip on top. The timescales of the correlations shown in Fig. 4.4 **b** show a different behaviour than we observed before and have a maximum shifted to negative laser detunings, which then again decays on both sides.

4.1.3 Biexciton coupling

To explain our observation of a small, laser-detuning-independent antibunching over an extended range of polariton energies, we have to introduce the coupling to an additional state. We expect this state to be spectrally broad and couple only weakly to the polariton, as we do not observe it in the polariton spectrum. While we can assume the presence of localized defects in

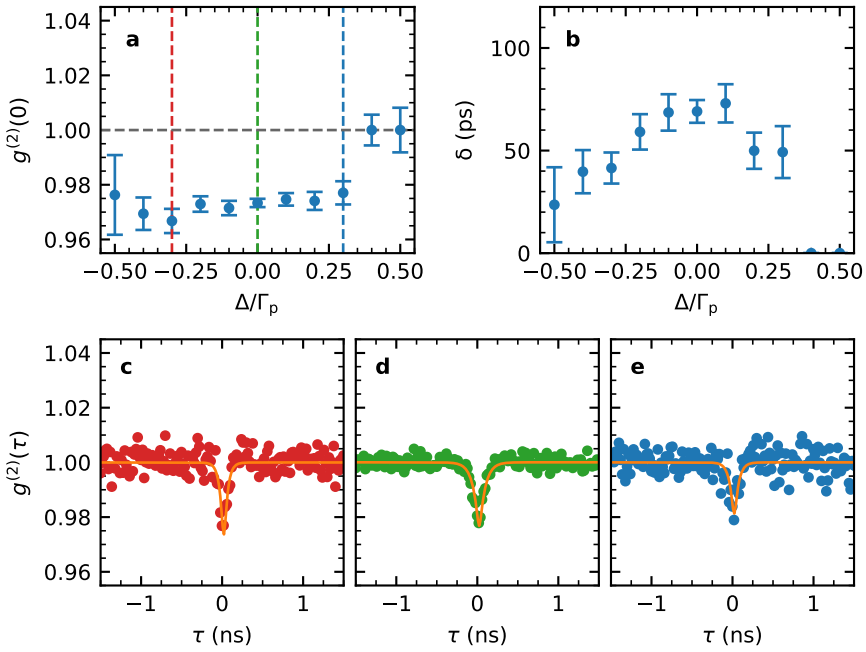

Figure 4.5: **a** Detuning dependence of $g^{(2)}(0)$ at $|c_c|^2 = 0.46$, **b** the corresponding timescales δ and **c** to **e** the measured $g^{(2)}(\tau)$ marked by vertical lines in **a**. The symmetric behaviour around $\Delta = 0$ is not captured by the basic polariton Hamiltonian (Eq. (2.15)) and suggests the coupling to another feature in the system with strong correlations. In Section 4.1.3 we explore the biexciton as a possible origin of this behaviour.

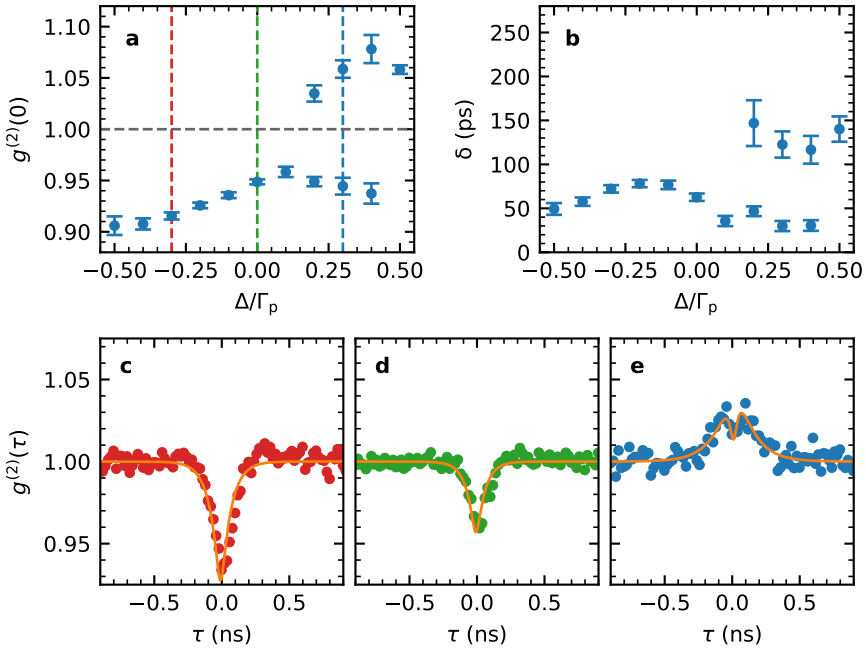

Figure 4.6: **a** Detuning dependence of $g^{(2)}(0)$ at $|c_c|^2 = 0.34$, **b** the corresponding timescales δ and **c** to **e** the measured $g^{(2)}(\tau)$ marked by vertical lines in **a**. We observe an intermediate behaviour compared to Figs. 4.4 and 4.5. While we see the expected behaviour on the red side (**c**), the dip does not vanish when approaching $\Delta/\Gamma_p = 0$ (**d**) and even remains on the blue side (**e**) on top of a bunching peak. To quantify both features, we separate the timescales of the dip and the peak and fit both separately, leading to the values shown in **a** and **b**. Comparing **b** with Fig. 4.4 **b**, we can see that the maximum of the blockade timescale is shifted by about $-0.25\,\Gamma_p$.

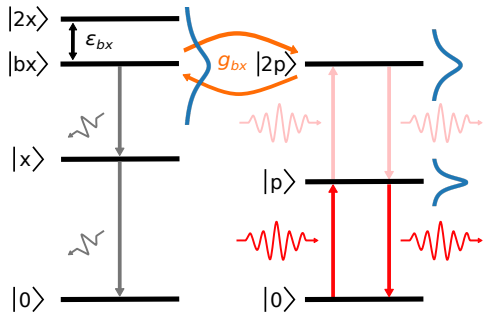

Figure 4.7: Illustration of the dissipative blockade mechanism. The biexciton $|bx\rangle$ couples to the two polariton state $|2p\rangle$, therefore leading to a substantial line broadening and a reduced overlap to the single excited polariton state $|p\rangle$.

the sample, they are unlikely candidates as they are expected to be energetically narrower then what we observe in the correlation measurements and if they couple strong enough to substantially modify the correlations they simultaneously lead to a modification of the polariton spectrum.

A more likely scenario is that we observe the influence of the biexciton, a bound state formed between two excitons. The coupling to the polariton and the resulting changes of the interactions were already theoretically described [41] and experimentally observed [42, 43]. In these experiments the presence of the bound biexciton state leads to a Feshbach resonance for the polariton scattering process which leads to a sign-change of the interactions as the polariton energy is tuned over the biexciton resonance. As there is no sign change in our observations, we propose a dissipative mechanism which has been theoretically explored in [89], based on the broad linewidth of the biexciton and the exclusive coupling to the doubly excited polariton state $|2p\rangle$. This leads to a selective line broadening of $|2p\rangle$ compared to $|p\rangle$ which reduces their overlap and thus the excitation probability of the doubly excited state. This "dissipative blockade" mechanism is independent of the detuning between the laser and the polariton and as the densities in our systems are low, the biexciton coupling is too weak to lead to modifications of the polariton spectrum.

To model the effects of the biexciton coupling and the resulting modifica-

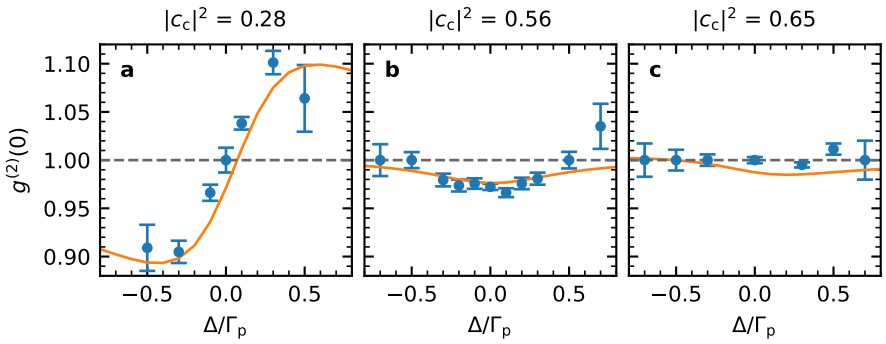

Figure 4.8: Simulated correlations (orange) including the coupling to the biexciton for three different cavity contents and the corresponding data. The calculated values describe the detuning-independent antibunching well (**b**), while only leading to slight deviations at high (**c**) and low (**a**) cavity content, where the correlations are dominated by the coherence of the laser or the polariton interactions.

tion of the correlations, we add

$$H_{\mathrm{bx}} = E_{\mathrm{bx}} b^\dagger b + g_{\mathrm{bx}} \left(b^\dagger pp + bp^\dagger p^\dagger \right) \tag{4.2}$$

to the polariton Hamiltonian and calculate $g^{(2)}$ using numerical simulations (for more details on the simulations see Appendix A). In the above expression, b is the biexciton annihilation operator and g_{bx} the corresponding coupling strength. The energy of the biexciton is thereby determined by the biexciton binding energy, $E_{\mathrm{bx}} = 2E_{\mathrm{dx}} - \varepsilon_{\mathrm{bx}}$. Since we mainly aim for a proof of concept and the biexciton parameters are not exactly known, we orient ourselves along the parameters in [42, 43] and adjust them to match the result of the model to the data. In more detail this means that we first set the polariton interactions to zero and adjust the biexciton parameters to reproduce the detuning-independent antibunching around $|c_c|^2 = 0.5$ and only weakly affect the correlations at $|c_c|^2 = 0.28$ and $|c_c|^2 = 0.65$. Then we set U_{pp} to match the result of the simulations with the data. We find a good agreement with the data for the parameters shown in Table 4.1 and the polariton interaction strengths shown in Fig. 4.9 **b**, where the value at $|c_c|^2 = 0.28$ is slightly lower then what we extracted from the fit without biexciton shown in

	This work	Takemura 2014 [42]	Scarpelli 2024 [43]
$\varepsilon_{\mathrm{bx}}$	2.6 meV	3 meV	2.2 meV
γ_{bx}	0.9 meV	1.1 meV	0.34 meV
g_{bx}	8 µeV	360 µeV$/\sqrt{n_{\mathrm{p}}}$	70 µeV

Table 4.1: Values for the biexciton binding energy $\varepsilon_{\mathrm{bx}}$, linewidth γ_{bx} and coupling strength g_{bx} used in this work and in the literature. The different coupling strengths originate most likely from the differed polariton densities in the three experiments.

Fig. 4.4 **a**. In Fig. 4.8 we show the detuning-dependent correlations for three different cavity contents together with the simulations using the parameters described above. They agree well with the laser-detuning-independent antibunching (Fig. 4.8 **b**) while for large cavity content the coherence of the laser (Fig. 4.8 **c**) and for small cavity content the correlations induced by polariton interactions (Fig. 4.8 **a**) remain only sightly perturbed. The overall $|c_{\mathrm{c}}|^2$ dependence in Fig. 4.9, shows a good agreement between the data and the simulation results.[2] The orange color gradient and the blue line show the extend of the biexciton.

While the interaction strengths at lower cavity content $|c_{\mathrm{c}}|^2 < 0.4$ lay well within the range of values found in literature (Fig. 4.10), the decrease of the interaction strength with increased cavity content (Fig. 4.9 **b**) happens faster then we would expect from a simple Hopfield coefficient argument, where $U_{\mathrm{pp}} = |c_{\mathrm{dx}}|^4 U_{\mathrm{xx}}$. Recent theoretical work [83] describes the interactions between dipolar polaritons in a 1D channel using a microscopic model. They find that the polariton interaction strength is greatly enhanced compared to results from perturbative theories, originating from the fact that the polariton mass is orders of magnitudes lower than the exciton mass. This strongly modifies the interaction strength as a function of cavity–exciton detuning, resulting in a relatively sharp maximum around zero detuning compared to the continuous change described by the quadratic formula in Eq. (2.23). While this model does not describe the 2D direct exciton–polaritons in our system and we do not observe a maximum in the polariton interaction strength around $|c_{\mathrm{c}}|^2 = 0.5$, it strongly suggests that the argument based on Hopfield

[2] As we only know values for U_{pp} and Γ_{p} at the measured cavity contents, the simulation results are interpolated for better visibility.

coefficients alone is not sufficient to describe polariton interactions and the role of strong light–matter coupling has to be regarded.

Although we cannot explain the dependence of U_{pp}, the good agreement between the simulation and the data using reasonable parameters for the biexciton coupling provides strong evidence that we observe a dissipative blockade mechanism, where selective coupling to a lossy state induces quantum correlations.

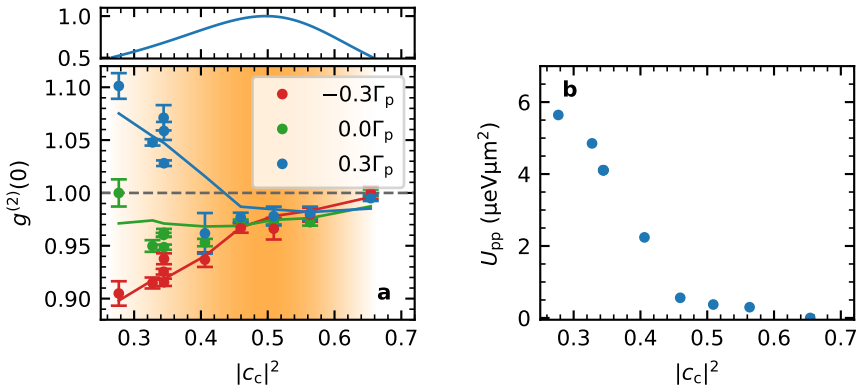

Figure 4.9: a Cavity content dependence as in Fig. 4.3, with solid lines showing simulation results. The width of the biexciton is indicated by the color gradient and the distribution above. The simulation reproduces the data reasonably well and mostly deviates for the resonant measurements around $|c_{\mathrm{c}}|^2 = 0.34$. **b** Values of the polariton interaction strength chosen for the theoretical calculations to match the experimental data. While the values lay within a reasonable range, the dependence is steeper than we would expect from $U_{\mathrm{pp}} = |c_{\mathrm{dx}}|^4 U_{\mathrm{xx}}$.

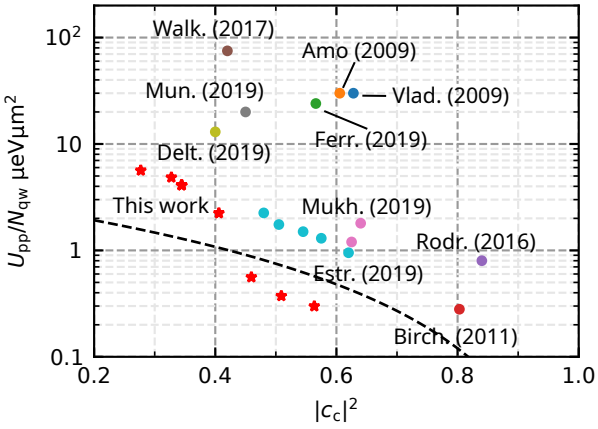

Figure 4.10: Polariton–polariton interaction strengths in different experiments over the past 15 years, compared with our values (red stars). The black dashed line indicates the values of $U_{pp} = |c_{dx}|^4 U_{xx}/2$ where $U_{xx} = 6\,\mu eV\mu m^2$ is calculated using the Born approximation. Comparable to the values found by Estr. (2019) and Birch. (2011) our values below $|c_c|^2 = 0.4$ lay about a factor of 2.5 above the theoretical line. [16, 46, 54, 55, 78–82]

4.2 Indirect exciton–polaritons

In the previous section we showed observations of nonclassical correlations induced by polariton interactions down to $g^{(2)}(0) = 0.9$. Our next step towards strongly correlated systems is the introduction of a finite permanent dipole through the indirect exciton content to enhance the polariton interactions.

As it turns out, the reduction in oscillator strength of the hybridised exciton due to the small overlap between the electron and hole wave function of the indirect exciton leads to larger line broadening and lower transmission than initially anticipated. In Fig. 4.11 we show the changes in both values normalized to the direct polariton as a function of the indirect exciton ratio $r_{\mathrm{ix}} = |c_{\mathrm{ix}}|^2 / \left(|c_{\mathrm{dx}}|^2 + |c_{\mathrm{ix}}|^2\right)$. The trend agrees with calculations assuming a cavity mode coupled to the inhomogeneously broadened lower exciton branch, whose light–matter coupling depends on the indirect exciton ratio, $\Omega_{\mathrm{eff}} = (1 - r_{\mathrm{ix}})\Omega$. It shows that the reduction in light–matter coupling weakens the "cavity protection" described in Section 2.3.3. This results in a reduction of the transmission already for small indirect exciton ratios and then for higher rations to a significant broadening.

This substantially lowers the range of parameters we can explore in the experiment and sets an upper limit to the indirect exciton ratio of the polaritons. We can estimate the interaction enhancement due to the dipolar nature by rewriting Eq. (2.23) and normalizing it by the bare exciton interaction and the cavity content,

$$\tilde{U}_{\mathrm{pp}} = \frac{U_{\mathrm{pp}}}{U_{\mathrm{dxdx}}(1 - |c_{\mathrm{c}}|^2)^2} = (1 - r_{\mathrm{ix}})^2 + \frac{U_{\mathrm{ixix}}}{U_{\mathrm{dxdx}}} r_{\mathrm{ix}}^2, \tag{4.3}$$

where we neglect the contribution of U_{dxix} as it is expected to be an order of magnitude smaller then the other two terms. In Fig. 4.12 we show the corresponding curves for $U_{\mathrm{ixix}} = 1.5\, U_{\mathrm{dxdx}}$ as theoretically predicted in [65] and $U_{\mathrm{ixix}} = 7.4\, U_{\mathrm{dxdx}}$ as extracted from measurements in [44]. It becomes clear that a minimal indirect exciton ratio is necessary to overcome the initial reduction of the interaction strength due to the reduced direct exciton nature. Even using the more optimistic value, an indirect exciton ratio of more than 30 % is necessary to observe an enhancement. At this indirect exciton ratio we already see a significant drop in transmission (Fig. 4.11 **b**) by about 50 %.

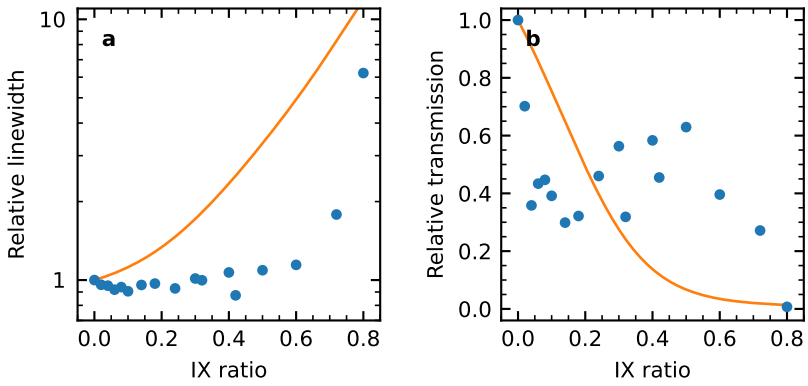

Figure 4.11: Relative change of the linewidth and transmission as function of the indirect exciton ratio at a constant cavity content $|c_c|^2 = 0.4$. The trend agrees with calculations assuming a cavity mode coupled to an inhomogeneously broadened lower exciton, with reduced light–matter coupling proportional to the indirect exciton ratio, $\Omega_{\text{eff}} = (1 - r_{\text{ix}})\Omega$. This suggests that the loss of oscillator strength makes the polariton more susceptible to the inhomogeneous broadening of the emitter.

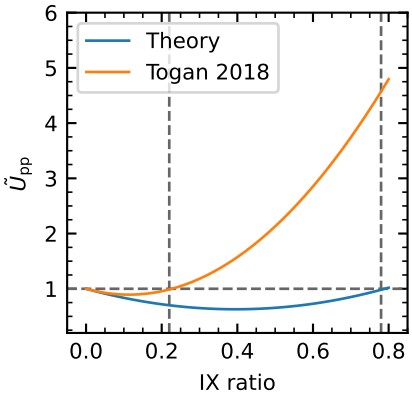

Figure 4.12: Enhancement of the normalized polariton interaction strength $\tilde{U}_{\text{pp}}$ as a function of the indirect exciton ratio. Using values from theoretical predictions $U_{\text{ixix}} = 1.5\,U_{\text{dxdx}}$ [65], and the findings from [44] $U_{\text{ixix}} = 7.4\,U_{\text{dxdx}}$, leads to different scalings but suggests that at a sizable indirect exciton ratio is necessary to enhance the interactions substantially.

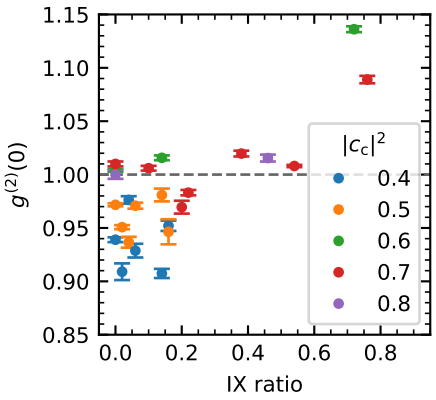

Figure 4.13: Summary of correlation measurements with different cavity contents as a function of the indirect exciton ratio. While we see nonclassical correlations in multiple measurements below 30 % indirect exciton ratio, above that the narrow band in parameter space with low linewidth and sufficient transmission makes measurements difficult and we were unable to observe antibunching.

In Fig. 4.13 we show a representative overview of measurements done with finite indirect exciton ratios. For small ratios we do not expect an enhancement of the interactions but the transmission and linewidth are still favorable to perform measurements, resulting in multiple data points with nonclassical correlations. For higher ratios where we expect an enhancement of the interactions, the low transmission only allowed for measurements with high cavity content and therefore no sizable antibunching was observed. The origin of the strong bunching features observed at high indirect exciton ratios in Fig. 4.13 is not clear, and we cannot say if it is due to some spurious correlations from the sample or if it originates from the indirect exciton.

In order to compensate for the reduction in oscillator strength at finite indirect exciton ratios, we designed and fabricated a second sample with three sets of QW pairs, each located at an antinode of the cavity. While this lowers the polariton interaction strength by a factor of three, our estimates suggested that the normal mode splitting which is increased by a factor of $\sqrt{3}$ allows for a larger indirect exciton fraction before the inhomogeneous broadening becomes to detrimental. This could potentially compensate for

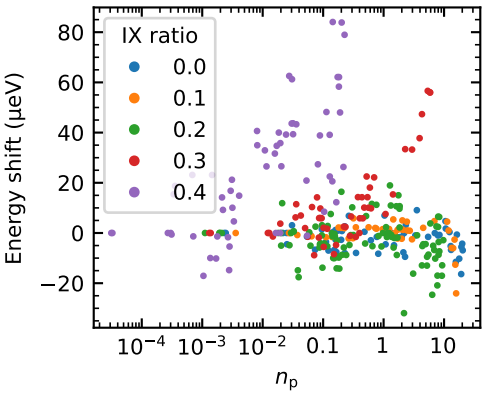

Figure 4.14: Energy shift of the polariton resonance as a function of the density for different indirect exciton ratios at $|c_c|^2 = 0.7$. The redshift visible at low indirect exciton contents makes the quantitative analysis of the data difficult. But qualitatively it clearly shows an increasing blueshift with $r_{ix} > 20\,\%$, underlining the presence of interactions that increase with the indirect exciton ratio.

the weaker interaction strength. Characterisations of the polariton spectrum of the second sample showed the expected larger coupling strength of $\Omega = 1.9\,\mathrm{meV}$ and the narrow polariton linewidths down to $\Gamma_p = 11\,\mu\mathrm{eV}$ indeed show the reduced coupling to the inhomogeneous exciton distribution. Through the low linewidth and potentially higher exciton content we can estimate that, despite the reduced interaction strength, antibunching dips of 5 % to 10 % can be expected even for direct exciton–polaritons. Regardless of these favorable conditions, we did not observe nonclassical correlations in this sample.

To ensure the presence of interactions, we spectroscopically probed the energy shift of the polariton resonance as function of the input power shown in Fig. 4.14. We could observe a sizable blueshift $\Delta E \approx g_{pp} n_p^2$ of the mode consistent with the repulsive polariton interactions. This blueshift is superimposed by a redshift of the mode which on one hand depends on the density of polaritons, but also directly on the input power. This suggests photon absorption in the system with two different contributions, one from photons inside the cavity mode and one of photons that do not couple to the

mode and therefore do not contribute to the polariton density. This twofold dependence hampers the calibration of the redshift and we could not extract quantitative information from these measurements. In Fig. 4.14 we show the energy shift as function of the polariton density for $|c_c|^2 = 0.7$ and different indirect exciton ratios. While below 30 % indirect exciton fraction, we only observe the aforementioned redshift, above we clearly see an increasing blueshift. Our data therefore qualitatively agrees with the findings in [44]. In these measurements we therefore observe nonlinear behaviour for a range of parameters, indicating that there has to be a to us unknown effect interfering with the correlations in this system.

Chapter 5
Summary and outlook

In this work we demonstrated the occurrence of nonclassical correlations in exciton–polaritons originating from the interactions inherited by their excitonic fraction. This was made possible by using a postselection scheme to overcome the fluctuations induced by the open cavity design which is necessary to have free tunability of the cavity energy. By comparing the correlations and polariton line shape at various indirect exciton contents, we could show that in our sample the gain in interactions due to the dipolar nature is not strong enough to overcome the loss in oscillator strength. The linewidth and transmission are affected by the proximity to the inhomogeneous exciton distribution, effectively limiting the observable parameter space to low indirect exciton contents, where the dipolar enhancement is not yet sizable. Therefore, to utilize the potential behind dipolar interactions, the quality of the sample has to be improved by either reducing the inhomogeneity of the excitons or by increasing the light–matter coupling. While we did not expect a substantial net gain in interaction strength by combining multiple QW pairs due to the delocalisation of the polaritons over the multiple QW pairs, the larger normal mode splitting could have allowed us to investigate the change of the interaction strength due to the indirect exciton. For unknown reasons we could not observe nonclassical correlations in the experiment, despite the sizable interaction induced blueshift.

On the other hand our measurements with purely direct exciton–polaritons showed the first observation of nonclassical correlations in polaritons using continuous wave excitation with a value $g^{(2)}(0) = 0.90(1)$ at $|c_c|^2 = 0.3$. We attribute this enhancement compared to previous measurements [54, 55] to the improved sample quality and the presence of the gate structure which reduces the amount of charge accumulation that potentially broadens the cavity linewidth. At lower exciton fractions we found a laser-detuning-

independent antibunching for several parameter settings, which cannot be explained by polariton interactions alone. As both processes lead to substantially different signatures in $g^{(2)}$ we can still extract a value for the polariton interaction strength $U_{\mathrm{pp}} = 5.2\,\mu\mathrm{eV}\mu\mathrm{m}^2$ providing an alternative data point to the polariton interaction strength found in other experiments, which to first order is independent of the polariton density.

We attribute the laser-detuning-independent correlations to the selective coupling of the biexciton to the doubly excited polariton state. The short lifetime of the biexciton leads to a reduced excitation probability of the doubly excited state and hence a reduced probability for emitting two simultaneous photons. Our numerical simulations match well with the data, suggesting the first observation of this dissipative blockade effect and allow us to extract the polariton interaction strength for different cavity contents. It thereby shows a stronger dependency on the cavity content than what we would expect from the quadratic Hopfield type argument, suggesting that a microscopic theory might be necessary to capture the details of the scaling. As the effect of the biexciton on the polariton interactions has so far only been observed as a Feshbach resonance [42, 43], further experiments investigating the dependence of the dissipative blockade on the biexciton coupling and linewidth should shed more light on this effect and could show its potential, for example as a source of single photons.

The correlations measured on this device are stronger than in previous observations and in principle only a reduction of the linewidth or area by a factor of 5 would be necessary to reach the strongly interacting regime where $g_{\mathrm{pp}} > \Gamma_{\mathrm{p}}$. The improvement by a factor of 5 could be possible by refining sample quality and design, but reaching it poses a technical challenge, for example as the effect of fluctuations would be more substantial for narrower linewidths.

One way of increasing the quality of the cavity is by surface passivation, which already showed a substantial increase in the cavity Q factor in [90]. Removing the natural GaAs oxide layer on the surface and protecting it with Al_2O_3 prevents the build-up of an electric field between the p-doped layer and the surface, which leads to absorption of the electromagnetic field inside the cavity.

The MBE growth of the bottom AlAs/GaAs DBR poses another limitation for this device structure. The growth of multiple layers with different

lattice constants introduces strain in the structure which eventually relaxes by disrupting the crystal lattice. In the current device the number of DBR layers is chosen as a compromise between the resulting inhomogeneity and the reflectivity of the mirror. Therefore, epitaxial liftoff [91, 92] to transfer the semiconductor QW onto a dielectric Ta_2O_5/SiO_2 DBR mirror could be used to replace the bottom semiconductor DBR. While this technique could potentially lead to new issues due to the introduction of new surfaces, it would allow for a narrower cavity linewidth and reduce the inhomogeneous broadening of the exciton.

In order to reduce the mode area, a different approach would be to electrostatically confine the excitons, which has recently been shown in transition metal dichalcogenides [93]. While this is not feasible for direct excitons in InGaAs due to the weak tunability via the dc Stark effect and the lower exciton binding energy found in transition metal dichalcogenide monolayers, the dipolar nature of the indirect exciton could provide enough leverage to introduce electrostatic confinement. To define the confined regions, the top gate would have to be patterned, for example by directly etching away the p-doped layer or by replacing it with a conductive material like indium tin oxide which can be structured using lithographic techniques. To determine the optimal area of the confinement one would have to consider the gain of g_{pp} compared to the reduction in oscillator strength. Additionally, by fabricating the regions smaller than the length scales of the inhomogeneity in the sample, one could also reduce the width of the inhomogeneous distribution of the excitons. The technical limit for such a structure is most likely the conductance through narrow channels which limits the patterning of the p-doped layer to roughly 100 nm, which would mean more than an order of magnitude reduction of the area.

Appendix A

Numerical simulations

To describe the polaritons in our system, we include the coupling to the biexciton state into the Hamiltonian in second quantized form,

$$\begin{aligned} H = &- \Delta p^\dagger p + \frac{g_{\mathrm{pp}}}{2} p^\dagger p^\dagger p p + F^* p^\dagger + F p \\ &- \Delta_{\mathrm{bx}} b^\dagger b + g_{\mathrm{bx}} \left(b^\dagger p p + b p^\dagger p^\dagger \right), \end{aligned} \tag{A.1}$$

together with the master equation

$$\frac{\partial \rho}{\partial t} = \mathcal{L}\rho \tag{A.2}$$

and the corresponding Liouvillian

$$\begin{aligned} \mathcal{L} = &- \frac{i}{\hbar} [H, \rho] + \frac{\Gamma_{\mathrm{p}}}{2} \left(2 p \rho p^\dagger - p^\dagger p \rho - \rho p^\dagger p \right) \\ &+ \frac{\gamma_{\mathrm{bx}}}{2} \left(2 b \rho b^\dagger - b^\dagger b \rho - \rho b^\dagger b \right). \end{aligned} \tag{A.3}$$

To solve these equations numerically we use QuTip [94, 95], an open-source toolbox for python designed to simulate dynamical quantum systems.

By defining the dimension $N_{\mathrm{p}} \otimes N_{\mathrm{bx}}$[1] of the Hilbert space, the toolbox allows us the write the Hamiltonian A.1 in second quantization while internally calculating the corresponding matrix representation. In a second step a build-in steady-state solver calculates the corresponding Liouvillian using the corresponding collapse operators $\sqrt{0.5\,\Gamma_{\mathrm{p}}}\,p$ and $\sqrt{0.5\,\gamma_{\mathrm{bx}}}\,b$, and solves for

[1] Except for the power-dependent simulations in Section 4.1.1, we are interested in low polariton densities. Therefore the dimension of the Hilbert space is set to $N_{\mathrm{p}} = N_{\mathrm{bx}} = 5$ to reduce computation time.

the steady-state density matrix ρ_{ss} satisfying $\mathcal{L}\rho_{\mathrm{ss}} = 0$ using factorisation. To then calculate the second-order correlation function

$$g^{(2)}(\tau) = \frac{\left\langle p^{\dagger}(0)p^{\dagger}(\tau)p(\tau)p(0)\right\rangle}{n_{\mathrm{p}}^2}, \tag{A.4}$$

where n_{p} is the polariton number, the toolbox offers a master equation solver which integrates Eq. (A.2) for given times τ and then calculates the correlations. We can assume the polaritons to be in the steady state, therefore the initial state for the integration is ρ_{ss} and since we are interested in $g^{(2)}(\tau = 0)$ we only integrate over short timescales to reduce the computation time. In the last step we normalize the correlations by n_{p}^2 obtained by calculating the expectation value $\langle n_{\mathrm{p}}\rangle = \mathrm{Tr}\Big\{\rho_{\mathrm{ss}}p^{\dagger}p\Big\}$.

Appendix B

Growth structure

The samples in this thesis were grown with MBE by Dr. Stefan Fält at the Advanced Semiconductor Quantum Materials group led by Prof. Werner Wegscheider at ETH Zürich. The layer structures of the two samples used in this thesis are shown in Tables B.1 and B.2. The structure is designed for optimal optical properties, therefore the doped layers are placed in nodes of the cavity mode to minimize absorption and the QW pair in an antinode to maximise the light–matter coupling. To minimize the amount of current flowing through the structure when applying a static electric field between the doped layers we introduce AlGaAs/GaAs superlattices which act as tunnel barriers due to their higher band gap. In the sample with three QW pairs additional tunnel blocking layers were introduced between the pairs to prevent charge transfer between them. In this structure the dopants are introduced in AlGaAs next to thin GaAs layers, into which the excess electrons and holes tunnel. This allows us to place the shallow defects related to the incorporation of the dopants in the higher band gap material with the intention to reduce the absorption. A corresponding reduction of the cavity linewidth compared to the previous sample could not be observed. The additional AlGaAs shown in Table B.2 is introduced to smoothen the growth of the structure.

Layer	Thickness (nm)	Material	Repetitions
Spacer	40	GaAs	
p-doping	40	GaAs	
Spacer	99.7	GaAs	
Tunnel block	3	AlGaAs	
Spacer	1	GaAs	
Tunnel block	40	AlGaAs	
Spacer	6.4	GaAs	
QW	10	InGaAs	
QW separation	11.8	GaAs	
QW	4.6	InGaAs	
Spacer	105.7	GaAs	
Tunnel block	7	AlGaAs	×10
Tunnel block	3	GaAs	
Spacer	23.2	GaAs	
n-doping	30	GaAs	
Spacer	44.9	GaAs	
DBR	72.2	AlAs	×34
DBR	59.6	GaAs	
Buffer		GaAs	

Table B.1: Growth design of the single QW pair sample used for most of this thesis.

Layer	Thickness (nm)	Material	Repetition
Spacer	52.5	GaAs/AlGaAs	
p-doping	17.8	GaAs/AlGaAs	
Tunnel block	6.6	AlGaAs	×10
Tunnel block	2.8	GaAs	
Spacer	19.1	GaAs/AlGaAs	
Spacer	30	GaAs/AlGaAs	
Tunnel block	14.2	AlGaAs	
Spacer	6.6	GaAs	
QW	10.4	InGaAs	
QW separation	12.2	GaAs	×3
QW	4.7	InGaAs	
Spacer	6.6	GaAs	
Tunnel block	14.2	AlGaAs	
Spacer	23.2	GaAs/AlGaAs	
Spacer	1.4	GaAs	
Tunnel block	6.6	AlGaAs	×24
Tunnel block	2.8	GaAs	
Spacer	7.7	AlGaAs	
n-doping	17.8	GaAs/AlGaAs	
Spacer	52.7	GaAs/AlGaAs	
DBR	72.2	AlAs	×34
Buffer		GaAs	

Table B.2: Growth design of the tripel QW pair sample.

Bibliography

[1] D. E. Chang, V. Vuletić, and M. D. Lukin, Quantum nonlinear optics - Photon by photon, *Nature Photonics* **8**, 685–694 (2014).

[2] H. J. Kimble, The quantum internet, *Nature* **453**, 1023–1030 (2008).

[3] V. Giovannetti, S. Lloyd, and L. Maccone, Advances in quantum metrology, *Nature Photonics* **5**, 222–229 (2011).

[4] A. Muthukrishnan, M. O. Scully, and M. S. Zubairy, Quantum microscopy using photon correlations, *Journal of Optics B: Quantum and Semiclassical Optics* **6**, 575–582 (2004).

[5] N. Gisin, G. Ribordy, W. Tittel, and H. Zbinden, Quantum cryptography, *Reviews of Modern Physics* **74**, 145 (2002).

[6] D. Bouwmeester, A. Ekert, and A. Zeilinger, *The Physics of Quantum Information* (Springer, Berlin, Heidelberg, 2000).

[7] P. A. Franken and J. F. Ward, Optical harmonics and nonlinear phenomena, *Reviews of Modern Physics* **35**, 23 (1963).

[8] P. A. Franken, A. E. Hill, C. W. Peters, and G. Weinreich, Generation of optical harmonics, *Physical Review Letters* **7**, 118–119 (1961).

[9] D. N. Basov, A. Asenjo-Garcia, P. J. Schuck, X. Zhu, and A. Rubio, Polariton panorama, *Nanophotonics* **10**, 549–577 (2020).

[10] A. Kavokin, *Microcavities* (Oxford University Press, 2011).

[11] J. M. Raimond, M. Brune, and S. Haroche, Manipulating quantum entanglement with atoms and photons in a cavity, *Reviews of Modern Physics* **73**, 565 (2001).

[12] P. R. Berman, *Cavity quantum electrodynamics* (Academic Press, Inc., Boston, MA (United States), 1994).

[13] J. J. Hopfield, Theory of the contribution of excitons to the complex dielectric constant of crystals, *Physical Review* **112**, 1555 (1958).

[14] C. Weisbuch, M. Nishioka, A. Ishikawa, and Y. Arakawa, Observation of the coupled exciton-photon mode splitting in a semiconductor quantum microcavity, *Physical Review Letters* **69**, 3314 (1992).

[15] J. Kasprzak, M. Richard, S. Kundermann, A. Baas, P. Jeambrun, J. M. Keeling, F. M. Marchetti, M. H. Szymánska, R. André, J. L. Staehli, V. Savona, P. B. Littlewood, B. Deveaud, and L. S. Dang, Bose-einstein condensation of exciton polaritons, *Nature* **443**, 409–414 (2006).

[16] A. Amo, J. Lefrère, S. Pigeon, C. Adrados, C. Ciuti, I. Carusotto, R. Houdré, E. Giacobino, and A. Bramati, Superfluidity of polaritons in semiconductor microcavities, *Nature Physics* **5**, 805–810 (2009).

[17] P. St-Jean, V. Goblot, E. Galopin, A. Lemaître, T. Ozawa, L. L. Gratiet, I. Sagnes, J. Bloch, and A. Amo, Lasing in topological edge states of a one-dimensional lattice, *Nature Photonics* **11**, 651–656 (2017).

[18] S. R. Rodriguez, W. Casteels, F. Storme, N. Carlon Zambon, I. Sagnes, L. Le Gratiet, E. Galopin, A. Lemaître, A. Amo, C. Ciuti, and J. Bloch, Probing a Dissipative Phase Transition via Dynamical Optical Hysteresis, *Physical Review Letters* **118**, 1–6 (2017).

[19] T. Fink, A. Schade, S. Höfling, C. Schneider, and A. İmamoğlu, Signatures of a dissipative phase transition in photon correlation measurements, *Nature Physics* **14**, 365–369 (2018).

[20] G. Nardin, G. Grosso, Y. Léger, B. Pietka, F. Morier-Genoud, and B. Deveaud-Plédran, Hydrodynamic nucleation of quantized vortex pairs in a polariton quantum fluid, *Nature Physics* **7**, 635–641 (2011).

[21] D. Sanvitto, S. Pigeon, A. Amo, D. Ballarini, M. De Giorgi, I. Carusotto, R. Hivet, F. Pisanello, V. G. Sala, P. S. Guimaraes, R. Houdré, E. Giacobino, C. Ciuti, A. Bramati, and G. Gigli, All-optical control of the quantum flow of a polariton condensate, *Nature Photonics* **5**, 610–614 (2011).

[22] A. Amo, S. Pigeon, D. Sanvitto, V. G. Sala, R. Hivet, I. Carusotto, F. Pisanello, G. Leménager, R. Houdré, E. Giacobino, C. Ciuti, and A. Bramati, Polariton superfluids reveal quantum hydrodynamic solitons, *Science* **332**, 1167–1170 (2011).

[23] G. Grosso, G. Nardin, F. Morier-Genoud, Y. Léger, and B. Deveaud-Plédran, Soliton instabilities and vortex street formation in a polariton quantum fluid, *Physical Review Letters* **107**, 245301 (2011).

[24] A. Imamoglu, H. Schmidt, G. Woods, and M. Deutsch, Strongly interacting photons in a nonlinear cavity, *Physical Review Letters* **79**, 1467–1470 (1997).

[25] A. Verger, C. Ciuti, and I. Carusotto, Polariton quantum blockade in a photonic dot, *Physical Review B* **73**, 1–4 (2006).

[26] K. M. Birnbaum, A. Boca, R. Miller, A. D. Boozer, T. E. Northup, and H. J. Kimble, Photon blockade in an optical cavity with one trapped atom, *Nature* **436**, 87–90 (2005).

[27] M. D. Eisaman, J. Fan, A. Migdall, and S. V. Polyakov, Invited review article: single-photon sources and detectors, *Review of Scientific Instruments* **82**, 71101 (2011).

[28] C. Couteau, S. Barz, T. Durt, T. Gerrits, J. Huwer, R. Prevedel, J. Rarity, A. Shields, and G. Weihs, Applications of single photons to quantum communication and computing, *Nature Reviews Physics* **5**, 326–338 (2023).

[29] S. Kako, C. Santori, K. Hoshino, S. Götzinger, Y. Yamamoto, and Y. Arakawa, A gallium nitride single-photon source operating at 200K, *Nature Materials* **5**, 887–892 (2006).

[30] T. Volz, A. Reinhard, M. Winger, A. Badolato, K. J. Hennessy, E. L. Hu, and A. İmamoğlu, Ultrafast all-optical switching by single photons, *Nature Photonics* **6**, 605–609 (2012).

[31] P. Michler, A. Kiraz, C. Becher, W. V. Schoenfeld, P. M. Petroff, L. Zhang, E. Hu, and A. Imamoğlu, A quantum dot single-photon turnstile device, *Science* **290**, 2282–2285 (2000).

[32] D. C. Burnham and D. L. Weinberg, Observation of simultaneity in parametric production of optical photon pairs, *Physical Review Letters* **25**, 84–87 (1970).

[33] M. P. Fisher, P. B. Weichman, G. Grinstein, and D. S. Fisher, Boson localization and the superfluid-insulator transition, *Physical Review B* **40**, 546 (1989).

[34] D. Jaksch, C. Bruder, J. I. Cirac, C. W. Gardiner, and P. Zoller, Cold bosonic atoms in optical lattices, *Physical Review Letters* **81**, 3108 (1998).

[35] M. Girardeau, Relationship between Systems of Impenetrable Bosons and Fermions in One Dimension, *Journal of Mathematical Physics* **1**, 516–523 (1960).

[36] M. Greiner, O. Mandel, T. Esslinger, T. W. Hänsch, and I. Bloch, Quantum phase transition from a superfluid to a mott insulator in a gas of ultracold atoms, *Nature* **415**, 39–44 (2002).

[37] T. Kinoshita, T. Wenger, and D. S. Weiss, Observation of a one-dimensional tonks-girardeau gas, *Science* **305**, 1125–1128 (2004).

[38] B. Paredes, A. Widera, V. Murg, O. Mandel, S. Fölling, I. Cirac, G. V. Shlyapnikov, T. W. Hansch, and I. Bloch, Tonks-Girardeau gas of ultracold atoms in an optical lattice, *Nature* **429**, 277–281 (2004).

[39] A. Amo and J. Bloch, Exciton-polaritons in lattices: a non-linear photonic simulator, *Comptes Rendus Physique* **17**, 934–945 (2016).

[40] C. Chin, R. Grimm, P. Julienne, and E. Tiesinga, Feshbach resonances in ultracold gases, *Reviews of Modern Physics* **82**, 1225–1286 (2010).

[41] I. Carusotto, T. Volz, and A. İmamoğlu, Feshbach blockade: Single-photon nonlinear optics using resonantly enhanced cavity polariton scattering from biexciton states, *Europhysics Letters* **90**, 37001 (2010).

[42] N. Takemura, S. Trebaol, M. Wouters, M. T. Portella-Oberli, and B. Deveaud, Polaritonic Feshbach resonance, *Nature Physics* **10**, 500–504 (2014).

[43] L. Scarpelli, C. Elouard, M. Johnsson, M. Morassi, A. Lemaitre, I. Carusotto, J. Bloch, S. Ravets, M. Richard, and T. Volz, Probing many-body correlations using quantum-cascade correlation spectroscopy, *Nature Physics* (2024).

[44] E. Togan, H.-T. Lim, S. Faelt, W. Wegscheider, and A. İmamoğlu, Enhanced Interactions between Dipolar Polaritons, *Physical Review Letters* **121**, 227402 (2018).

[45] C. Schneider, K. Winkler, M. D. Fraser, M. Kamp, Y. Yamamoto, E. A. Ostrovskaya, and S. Höfling, Exciton-polariton trapping and potential landscape engineering, *Reports on Progress in Physics* **80**, 016503 (2017).

[46] L. Ferrier, E. Wertz, R. Johne, D. D. Solnyshkov, P. Senellart, I. Sagnes, A. Lemaître, G. Malpuech, and J. Bloch, Interactions in confined polariton condensates, *Physical Review Letters* **106**, 126401 (2011).

[47] H. S. Nguyen, D. Vishnevsky, C. Sturm, D. Tanese, D. Solnyshkov, E. Galopin, A. Lemaître, I. Sagnes, A. Amo, G. Malpuech, and J. Bloch, Realization of a Double-Barrier Resonant Tunneling Diode for Cavity Polaritons, *Physical Review Letters*, 236601 (2013).

[48] C. Sturm, D. Tanese, H. S. Nguyen, H. Flayac, E. Galopin, A. Lemaître, I. Sagnes, D. Solnyshkov, A. Amo, G. Malpuech, and J. Bloch, All-optical phase modulation in a cavity-polariton Mach–Zehnder interferometer, *Nature Communications* **5**, 1–7 (2014).

[49] I. Rosenberg, Y. Mazuz-Harpaz, R. Rapaport, K. West, and L. Pfeiffer, Electrically controlled mutual interactions of flying waveguide dipolaritons, *Physical Review B* **93**, 195151 (2016).

[50] D. Liran, J. Hu, N. Lydick, H. Deng, L. Pfeiffer, and R. Rapaport, Electrically controlled dipolariton circuits, (2023), `arXiv:2308.08289`.

[51] B. Besga, C. Vaneph, J. Reichel, J. Estève, A. Reinhard, J. Miguel-Sánchez, A. İmamoğlu, and T. Volz, Polariton boxes in a tunable fiber cavity, *Physical Review Applied* **3**, 014008 (2015).

[52] T. Steinmetz, Y. Colombe, D. Hunger, T. W. Hänsch, A. Balocchi, R. J. Warburton, and J. Reichel, Stable fiber-based fabry-pérot cavity, *Applied Physics Letters* **89**, 111110 (2006).

[53] D. Hunger, T. Steinmetz, Y. Colombe, C. Deutsch, T. W. Hänsch, and J. Reichel, A fiber fabry–perot cavity with high finesse, *New Journal of Physics* **12**, 065038 (2010).

[54] A. Delteil, T. Fink, A. Schade, S. Höfling, C. Schneider, and A. İmamoğlu, Towards polariton blockade of confined exciton–polaritons, *Nature Materials* **18**, 219–222 (2019).

[55] G. Muñoz-Matutano, A. Wood, M. Johnsson, X. Vidal, B. Q. Baragiola, A. Reinhard, A. Lemaître, J. Bloch, A. Amo, G. Nogues, B. Besga, M. Richard, and T. Volz, Emergence of quantum correlations from interacting fibre-cavity polaritons, *Nature Materials* **18**, 213–218 (2019).

[56] T. Ihn, *Semiconductor nanostructures* (Oxford University Press, Oxford, 2010).

[57] M. E. Levinshtein and S. L. Rumyantsev, Gallium arsenide (GaAs), 77–103 (1996).

[58] G. Bastard, *Wave mechanics applied to semiconductor heterostructures*, Monographies de physique (Les Editions de Physique, 1988).

[59] D. Benoît, Q. Antonio, and P. Schwendimann, *Quantum coherence in solid state systems* (IOS Press, 2009).

[60] I. Carusotto and C. Ciuti, Quantum fluids of light, *Reviews of Modern Physics* **85**, 299–366 (2013).

[61] L. C. Andreani and A. Pasquarello, Accurate theory of excitons in GaAs-$Ga_{1-x}Al_x$ quantum wells, *Physical Review B* **42**, 8928–8938 (1990).

[62] W. W. Chow, S. W. Koch, and M. Sargent, *Semiconductor-laser physics* (Springer Berlin Heidelberg, 1994).

[63] G. Sek, J. Misiewicz, D. Radziewicz, M. Tłaczał, M. Panek, and R. Korbutowicz, Study of the nature of light hole excitonic transitions in InGaAs/GaAs quantum well, *Vacuum* **50**, 199–201 (1998).

[64] P. Cristofolini, G. Christmann, S. I. Tsintzos, G. Deligeorgis, G. Konstantinidis, Z. Hatzopoulos, P. G. Savvidis, and J. J. Baumberg, Coupling quantum tunneling with cavity photons, *Science* **336**, 704–707 (2012).

[65] T. Byrnes, G. V. Kolmakov, R. Y. Kezerashvili, and Y. Yamamoto, Effective interaction and condensation of dipolaritons in coupled quantum wells, *Physical Review B* **90**, 125314 (2014).

[66] A. V. Nalitov, D. D. Solnyshkov, N. A. Gippius, and G. Malpuech, Voltage control of the spin-dependent interaction constants of dipolaritons and its application to optical parametric oscillators, *Physical Review B* **90**, 235304 (2014).

[67] H. Deng, H. Haug, and Y. Yamamoto, Exciton-polariton bose-einstein condensation, *Reviews of Modern Physics* **82**, 1489–1537 (2010).

[68] N. Hodgson and H. Weber, *Laser Resonators and Beam Propagation*, Vol. 108, Springer Series in Optical Sciences (Springer New York, New York, NY, 2005).

[69] C. J. Sheppard, Approximate calculation of the reflection coefficient from a stratified medium, *Pure and Applied Optics: Journal of the European Optical Society Part A* **4**, 665 (1995).

[70] G. Panzarini, L. C. Andreani, A. Armitage, D. Baxter, M. S. Skolnick, V. N. Astratov, J. S. Roberts, A. Kavokin, M. Vladimirova, and M. A. Kaliteevski, Exciton-light coupling in single and coupled semiconductor microcavities: polariton dispersion and polarization splitting, *Physical Review B* **59**, 5082 (1999).

[71] S. Byrnes, tmm, `https://pypi.org/project/tmm/`.

[72] O. S. Heavens, Optical properties of thin films, *Reports on Progress in Physics* **23**, 1–65 (1960).

[73] J. Miguel-Sánchez, A. Reinhard, E. Togan, T. Volz, A. İmamoğlu, B. Besga, J. Reichel, and J. Estève, Cavity quantum electrodynamics with charge-controlled quantum dots coupled to a fiber fabry–perot cavity, *New Journal of Physics* **15**, 045002 (2013).

[74] H. Benisty, C. Weisbuch, J.-M. Gérard, R. Houdré, and J. Rarity, *Confined photon systems*, edited by H. Benisty, C. Weisbuch, É. Polytechnique, J.-M. Gérard, R. Houdré, and J. Rarity, Vol. 531 (Springer Berlin Heidelberg, 1999).

[75] H. J. Carmichael, *Statistical methods in quantum optics 1* (Springer Berlin Heidelberg, 1999).

[76] I. Diniz, S. Portolan, R. Ferreira, J. M. Gérard, P. Bertet, and A. Auffèves, Strongly coupling a cavity to inhomogeneous ensembles of emitters: Potential for long-lived solid-state quantum memories, *Physical Review A* **84**, 063810 (2011).

[77] C. Ciuti, V. Savona, C. Piermarocchi, A. Quattropani, and P. Schwendimann, Role of the exchange of carriers in elastic exciton-exciton scattering in quantum wells, *Physical Review B* **58**, 7926–7933 (1998).

[78] E. Estrecho, T. Gao, N. Bobrovska, D. Comber-Todd, M. D. Fraser, M. Steger, K. West, L. N. Pfeiffer, J. Levinsen, M. M. Parish, T. C. Liew, M. Matuszewski, D. W. Snoke, A. G. Truscott, and E. A. Ostrovskaya, Direct measurement of polariton-polariton interaction strength in the Thomas-Fermi regime of exciton-polariton condensation, *Physical Review B* **100**, 035306 (2019).

[79] A. S. Brichkin, S. I. Novikov, A. V. Larionov, V. D. Kulakovskii, M. M. Glazov, C. Schneider, S. Höfling, M. Kamp, and A. Forchel, Effect of Coulomb interaction on exciton-polariton condensates in GaAs pillar microcavities, *Physical Review B* **84**, 195301 (2011).

[80] S. Mukherjee, D. M. Myers, R. G. Lena, B. Ozden, J. Beaumariage, Z. Sun, M. Steger, L. N. Pfeiffer, K. West, A. J. Daley, and D. W. Snoke, Observation of nonequilibrium motion and equilibration in polariton rings, *Physical Review B* **100**, 245304 (2019).

[81] M. Vladimirova, S. Cronenberger, D. Scalbert, M. Nawrocki, A. V. Kavokin, A. Miard, A. Lemaître, and J. Bloch, Polarization controlled nonlinear transmission of light through semiconductor microcavities, *Physical Review B* **79**, 115325 (2009).

[82] P. M. Walker, L. Tinkler, B. Royall, D. V. Skryabin, I. Farrer, D. A. Ritchie, M. S. Skolnick, and D. N. Krizhanovskii, Dark Solitons in High Velocity Waveguide Polariton Fluids, *Physical Review Letters* **119**, 097403 (2017).

[83] E. R. Christensen, A. Camacho-Guardian, O. Cotlet, A. İmamoğlu, M. Wouters, G. M. Bruun, and I. Carusotto, Microscopic theory of cavity-enhanced interactions of dipolaritons, (2022), axXiv : 2212 . 02597v1.

[84] R. J. Glauber, The quantum theory of optical coherence, *Physical Review* **130**, 2529–2539 (1963).

[85] S. Ferretti and D. Gerace, Single-photon nonlinear optics with kerr-type nanostructured materials, *Physical Review B* **85**, 1–5 (2012).

[86] T. Fink, "Mean-Field and Quantum Interactions of Strongly Confined Exciton-Polaritons", PhD thesis (2018).

[87] K. Sivalertporn, L. Mouchliadis, A. L. Ivanov, R. Philp, and E. A. Muljarov, Direct and indirect excitons in semiconductor coupled quantum wells in an applied electric field, *Physical Review B* **85**, 45207 (2012).

[88] T. C. Liew and V. Savona, Multipartite polariton entanglement in semiconductor microcavities, *Physical Review A* **84**, 32301 (2011).

[89] A. Ben-Asher, A. I. Fernández-Domínguez, and J. Feist, Non-hermitian anharmonicity induces single-photon emission, *Physical Review Letters* **130**, 10.1103/PhysRevLett.130.243601 (2023).

[90] D. Najer, N. Tomm, A. Javadi, A. R. Korsch, B. Petrak, D. Riedel, V. Dolique, S. R. Valentin, R. Schott, A. D. Wieck, A. Ludwig, and R. J. Warburton, Suppression of Surface-Related Loss in a Gated Semiconductor Microcavity, *Physical Review Applied* **15**, 44004 (2021).

[91] C. W. Cheng, K. T. Shiu, N. Li, S. J. Han, L. Shi, and D. K. Sadana, Epitaxial lift-off process for gallium arsenide substrate reuse and flexible electronics, *Nature Communications* **4**, 1577 (2013).

[92] L. Greuter, D. Najer, A. V. Kuhlmann, S. R. Valentin, A. Ludwig, A. D. Wieck, S. Starosielec, and R. J. Warburton, Epitaxial lift-off for solid-state cavity quantum electrodynamics, *Journal of Applied Physics* **118**, 75705 (2015).

[93] D. Thureja, A. İmamoğlu, T. Smoleński, I. Amelio, A. Popert, T. Chervy, X. Lu, S. Liu, K. Barmak, K. Watanabe, T. Taniguchi, D. J. Norris, M. Kroner, and P. A. Murthy, Electrically tunable quantum confinement of neutral excitons, *Nature* **606**, 298–304 (2022).

[94] J. R. Johansson, P. D. Nation, and F. Nori, QuTiP: An open-source Python framework for the dynamics of open quantum systems, *Computer Physics Communications* **183**, 1760–1772 (2012).

[95] J. R. Johansson, P. D. Nation, and F. Nori, QuTiP 2: A Python framework for the dynamics of open quantum systems, *Computer Physics Communications* **184**, 1234–1240 (2013).

List of figures

Contributions

During various stages of this thesis, several people contributed to this work. The design of the cavity is based on the works of Dr. Thomas Volz and Dr. Andreas Reinhard. Dr. Thomas Fink manufactured and characterized the dimpled fibers, and was involved in the early stages of designing and building the setup. The samples where grown by Dr. Stefan Fält at the "Advanced Semiconductor Quantum Materials" group at ETH Zürich led by Prof. Werner Wegscheider, and processed in collaboration with Dr. Emre Togan und Dr. Stefan Fält at the FIRST cleanroom facilities at ETH Zürich. The design and implementation of the postselection and stabilization procedure was done in collaboration with Dr. Patrick Knüppel. The programming of the redpitaya STEMlab125-14 FPGA was done by Yu Liu as a research project at the "Quantum Optics" group led by Prof. Tilman Esslinger at ETH.

A paper about the content of this thesis is currently in preparation.

Acknowledgements

I am deeply grateful for all my coworkers, friends and family who where, in many different ways, part of this journey, supported me on the way and made this thesis possible. And while it is difficult to summarize what you all have done for me, I would like to attempt so in a few words.

I would like to start by thanking my supervisor Ataç İmamoğlu, who took me in as a student and created this great environment where I could do my research. Sharing his deep understanding and enthusiasm of physics has been very inspiring and I always left our discussions with new insights or a different perspective on the problem. I would also like to thank my co-examiners Sylvain Ravets and Jérôme Faist to spend their time and efforts to examine my thesis and for the interesting discussions. My deep gratitude also goes to Martin Kroner, whose never ending support in and around the lab made it possible to overcome the daily obstacles occurring in an experiment and who shared with me his intuitive understanding of physics in countless discussions. I got though a lot by his pragmatic and hands on approach, and with his help setbacks or broken parts in the laboratory often turned into a chance to learn something new. I want to thank Patrick Knüppel who joint me on this project for a short but great time. His positive spirit and curiosity was always motivating and his work in the lab led to significant improvements of the experiment and to some of my most pleasant memories working on this project. I also thank Aymeric Delteil and Hyang-Tag Lim for introducing me to the fiber–cavity setup and Aymeric Delteil for many valuable discussions and great advice, Emre Togan who taught me a lot about sample fabrication, Thomas Fink who fabricated and characterized the dimpled fibers, Stefan Fält who grew the samples and Ulrich Czopak and Hamza Abudayyeh who joined my project during their short visit. Special thanks also goes to Manuela Weber-Semler for her amazing administrative

support and to the mechanical workshop and the laboratory support team, especially Isabelle Altorfer, Martin Klöckner and Sandro Tiegermann. Their invaluable work creates a smoothly running infrastructure that allowed me to focus on my research.

During this time, I had the pleasure to work in a research group with many amazing people who created great memories in and around the lab, at lunch or apéros, during movie nights or during climbing or hiking in the mountains. I want to thank all of you for these great memories and for creating a nice environment at work. I specially want to thank Livio Ciorciaro, for sharing this path through years of studies and PhD with me, for all the discussions and for always being a great friend, Olivier Huber, who shared with me the pains and pleasures of working with a fiber cavity and the love for mountaineering, Alperen Tüğen whose incredibly optimistic attitude brighten many days, Deepankur Thureja for his very professional but at the same time also very cool manner and Punnet Murthy and Thibault Chervy who where always there for insightful discussions but also to bring some life in our group. I also want to thank all the former and current members of the quantum photonics group for the great times: Ajit Srivastava, Sina Zeytinoğlu, Ido Schwartz, Yuta Tsuchimoto, Li Bing Tan, Alexander Popert, Francesco Colangelo, Ivan Amelio, Clemens Kuhlenkamp, Tomasz Smoleński, Natasha Kiper, Felix Helmrich, Tobia Nova, Bertrand Evrard, Igor Khanonkin, Takahiro Uto, Sahra Hiestand, Hayden Adlong and Emre Yazıcı.

I also want to express my gratitude to Andrea Bergschneider, for always standing beside me in my professional and personal life, for helping me keep my head together during stressful times and for just being an amazing person. I also want to thank the people who guided me onto this path, my high school teacher Christoph Murer, who nourished my interest in natural sciences and helped me choose my study direction and Kevanc Esat, who supervised my first academic research project where he introduced me to the joy of doing optical experiments and led me towards my current research direction. I also want to thank all my friends and flatmates for all the great times over all these years and for providing some much needed balance to my research: Claude Peter, Laurent Kaufman, Marc Burkhard, Pascal Christen, Dominik Glinz, Valentin Beck, Marc Rüedi, Stephanie Huwiler, Gianluca Janka, Raphael Etter, Christian Valensieck, Matthias Müller-Schrader, Fadri Grünenfelder,

Violeta de la Rosa, Lea Segner and Nisrina Sukriandi.

Special thanks also go to Livio Ciorciaro, Martin Kroner and Andrea Bergschneider for proof reading and providing me with great feedback on my thesis.

Finally I am deeply grateful to my parents Esther Rudin and Heribert Schnüriger, who always encouraged me to be curious and supported me on this new path. Thank you for always being there for me and for all your guidance.

Thank you all!